Graphical Models 78 (2015) 36–59

Contents lists available at ScienceDirect

Graphical Models

journal homepage: www.elsevier.com/locate/gmod

Balanced multiresolution for symmetric/antisymmetric filters ☆,☆☆

Mahmudul Hasan *, Faramarz F. Samavati, Mario C. Sousa

Department of Computer Science, University of Calgary, Alberta, Canada

A R T I C L E   I N F O

Article history:
Received 12 May 2014
Received in revised form 15 January 2015
Accepted 21 January 2015
Available online 3 February 2015

Keywords:
Multiresolution
Reverse subdivision
Balanced decomposition
Perfect reconstruction
Lossless reconstruction
Symmetric extension
Antisymmetric extension
Focus+context visualization
Contextual close-up

A B S T R A C T

Given a set of symmetric/antisymmetric filter vectors containing only regular multiresolution filters, the method we present in this article can establish a *balanced multiresolution* scheme for images, allowing their *balanced decomposition* and subsequent perfect reconstruction without the use of any extraordinary boundary filters. We define balanced multiresolution such that it allows balanced decomposition i.e. decomposition of a high-resolution image into a low-resolution image and corresponding *details* of equal size. Such a balanced decomposition makes on-demand reconstruction of *regions of interest* efficient in both computational load and implementation aspects. We find this balanced decomposition and perfect reconstruction based on an appropriate combination of symmetric/antisymmetric extensions near the image and detail boundaries. In our method, exploiting such extensions correlates to performing sample (pixel/voxel) split operations. Our general approach is demonstrated for some commonly used symmetric/antisymmetric multiresolution filters. We also show the application of such a balanced multiresolution scheme in real-time focus+context visualization.

1. Introduction

1.1. Context

Applications that facilitate multiscale 2D and 3D image visualization and exploration (see [17,34,28], for example) benefit from multiresolution schemes that decompose high-resolution images into low-resolution approximations and corresponding *details* (usually, wavelet coefficients). Several subsequent applications of such a decomposition constructs the corresponding *wavelet transform*. This wavelet transform can then be used to derive low-resolution approximations of the entire image, as well as high-resolution approximations of a *region of interest* (ROI), on demand. Reconstructing the high-resolution approximation of a ROI involves locating the corresponding details from a hierarchy of details within the wavelet transform. One such hierarchy of details resulting from only two levels of decomposition of an Earth image (data source: Visible Earth, NASA) is shown in Fig. 1.

For the purpose of demonstration, we created the wavelet transform in Fig. 1 using the *short* filters of quadratic B-spline presented by Samavati et al. [27,28]. In practice, images that require multiscale visualization are larger in size and may require more levels of decomposition. For each level of decomposition in this particular example, the image was first decomposed heightwise and then widthwise.

☆ Supported by the *Natural Sciences and Engineering Research Council* (NSERC) of Canada, *Alberta Innovates – Technology Futures* (AITF), *Alberta Enterprise and Advanced Education*, *Networks of Centres of Excellence* (NCE) of Canada in *Graphics, Animation and New Media* (GRAND), and the *NSERC/AITF/Foundation CMG Industrial Research Chair* program in *Scalable Reservoir Visualization*.
☆☆ This paper has been recommended for acceptance by Hao (Richard) Zhang and Peter Lindstrom.
* Corresponding author.
E-mail addresses: mhasan@ucalgary.ca (M. Hasan), samavati@ucalgary.ca (F.F. Samavati), smcosta@ucalgary.ca (M.C. Sousa).

http://dx.doi.org/10.1016/j.gmod.2015.01.001
1524-0703/

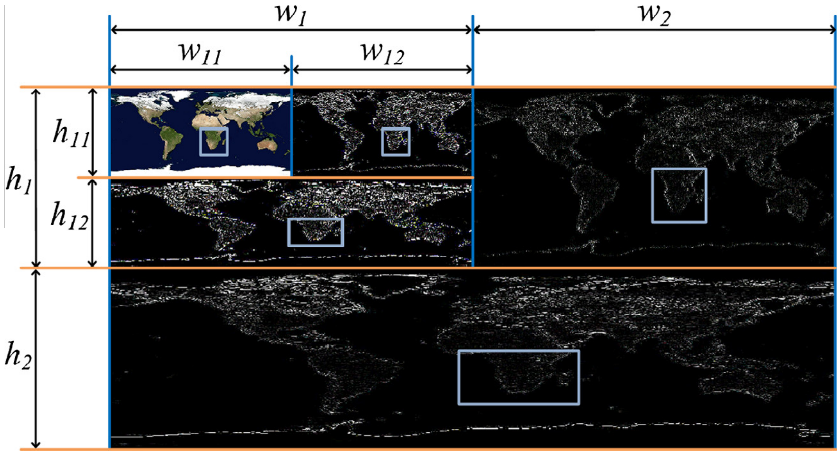

Fig. 1. Hierarchy of details in a wavelet transform resulting from two levels of decomposition of a 1024×512 Earth image. The coarse image (at the top left corner) contains a rectangular ROI and the details corresponding to that ROI are enclosed by rectangles within all levels of details.

1.2. Problem

Sequences of samples along each image dimension can be treated as finite-length signals. It is well-known that decomposition and reconstruction of finite-length signals require special treatments at the boundaries [1], which often involves the use of extraordinary boundary filters. The use of extraordinary boundary filters (as opposed to regular filters) for handling image and detail boundaries lead to computationally untidy reconstruction near image boundaries.

From a hierarchy of details, such as the one in Fig. 1, if we need to reconstruct the high-resolution approximation of a ROI located in the low-resolution (coarse) image shown in the top-left rectangle in Fig. 1, we have to locate the corresponding details in some or all of the rectangles that contain details depending on the expected level of resolution. Locating these details will be straightforward if each of the heightwise and widthwise decomposition steps decomposes an image into two halves of equal size – one half corresponding to the coarse image and the other half corresponding to the details. Among B-spline wavelets, only the filters obtained from Haar wavelets provide such a balanced decomposition [12,29]. However, because Haar wavelets and the associated scaling functions are not continuous, it would be beneficial to achieve such a balanced decomposition for the filters obtained from higher order scaling functions and their wavelets.

Existing multiresolution schemes for the local filters of second or higher order scaling functions and their wavelets (see [28,5,8,21], for example) result in unequal numbers of coarse and detail samples after decomposition (i.e. $w_1 \neq w_2, w_{11} \neq w_{12}, h_1 \neq h_2$, and $h_{11} \neq h_{12}$ in Fig. 1). Such inequalities resulting from decomposition make locating the details corresponding to a ROI for reconstruction a cumbersome task (which involves keeping track of level-wise offsets from boundaries), specially when an interactive multilevel visualization hierarchy (see Fig. 13(a), for example) is concerned. Creation of a such an interactive visualization hierarchy requires efficient on-demand access to details.

In contrast, balanced decompositions can construct *balanced wavelet transforms*, such as the one shown in Fig. 2 (data source: Visible Earth, NASA). In Fig. 2, the rectangles containing different levels of details for the entire image are numbered with $(l,1)$ tuples for widthwise and $(l,2)$ tuples for heightwise decompositions, where l represents the level of resolution. Locating the details corresponding to a ROI on demand in a balanced wavelet transform includes a number of simple dyadic operations, which are known to perform significantly faster than non-dyadic operations in both hardware and software implementations. Such efficient access to details is demonstrated by means of an example in Fig. 2. In general, if $c_{x,y}$ is the coarse sample at the top-left corner of a ROI rectangle, then $d^{(l,1)}_{2^{l-1}(w_c+x),2^{l-1}y}$ and $d^{(l,2)}_{2^l x,2^{l-1}(h_c+y)}$ are the detail samples at the top-left corners of the detail rectangles corresponding to the ROI for widthwise and heightwise balanced decompositions, respectively. Here, $w_c \times h_c$ ($\frac{w}{4} \times \frac{h}{4}$ in Fig. 2) is the resolution of the coarse image containing the ROI.

1.3. Proposed approach

In order to address the issues discussed above, in this article, we introduce a technique for devising *balanced multiresolution* schemes for the local filters of second or higher order scaling functions and their wavelets. Our technique uses an appropriate combination of symmetric/antisymmetric extensions near the image and detail boundaries, which correlate to sample split operations. To guarantee a perfect (lossless) reconstruction without the use of any extraordinary boundary filters, our method requires each of the given decomposition and reconstruction filter vectors (kernels) to be either symmetric or antisymmetric about their centers. Many existing sets of local regular multiresolution filters, such as those associated with the B-spline wavelets [28], biorthogonal and

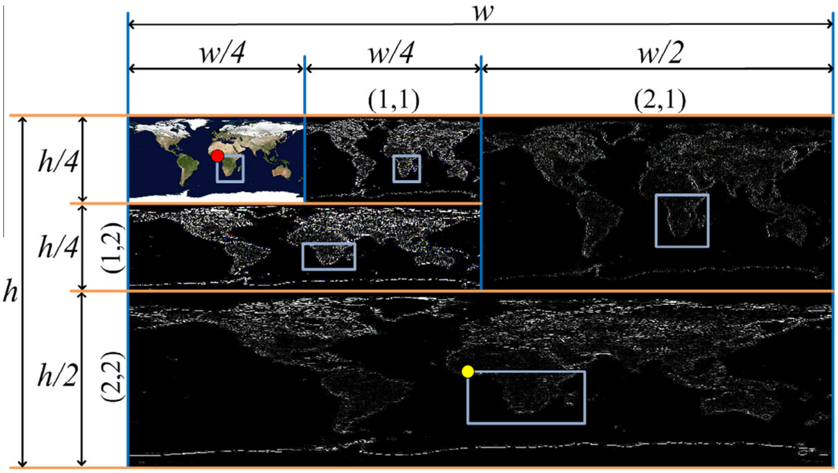

Fig. 2. A ROI in a balanced wavelet transform after two levels of balanced decompositions of a 1024×512 Earth image is shown. The location of the coarse sample highlighted with a red circle at top-left corner of the ROI rectangle in the coarse image is denoted (x, y). Due to balanced decompositions, the detail rectangles (four here) corresponding to the ROI can be found with simple dyadic operations. For example, the location of the detail sample highlighted with a yellow circle at top-left corner of the detail rectangle corresponding to the ROI is $\left(2^l x, 2^{l-1}(h/4 + y)\right)$, where the level of resolution $l = 2$. (For interpretation of the references to colour in this figure legend, the reader is referred to the web version of this article.)

reverse biorthogonal wavelets [5,8], and Meyer wavelets [21,8], exhibit such symmetric/antisymmetric structures.

1.4. Contributions

We present a novel method to devise a balanced multiresolution scheme for a given set of symmetric/antisymmetric multiresolution filter vectors containing regular filters. Devised balanced multiresolution schemes allow balanced decomposition and perfect reconstruction without the use of extraordinary boundary filters. A balanced wavelet transform representation of an image resulting from balanced decompositions provides straightforward and efficient access to previously extracted details corresponding to a ROI on demand. We also provide ready-to-use balanced multiresolution schemes devised using our proposed method for eleven commonly used sets of symmetric/antisymmetric multiresolution filter vectors (see Table A.2). Additionally, we show the application of a devised balanced multiresolution scheme in real-time multilevel focus+context visualization of large-scale 2D and 3D images. As opposed to in-place magnification of ROIs, the presented mode of focus+context visualization uses contextual close-ups to display spatially separate magnification of ROIs constructed through perfect reconstructions.

1.5. Article roadmap

This article is organized as follows. In Section 2, we present the notations used throughout the article. Next, we formulate the problem definition in Section 3, which is followed by a brief survey of the existing related work in Section 4. Section 5 presents our method for devising a balanced multiresolution scheme accompanied by two examples – one for odd-length and the other for even-length decomposition filter vectors. We demonstrate the application of a balanced multiresolution scheme devised by our method in real-time focus+context visualization with experimental results in Section 6. In Section 7, we discuss with examples what may lead to unwanted extraordinary boundary reconstruction filters and highlight some characteristics of our method with possible directions for future work. Finally, Section 8 concludes the article. We also provide two appendices with additional examples of balanced multiresolution schemes devised by our method.

2. Notation

2.1. Multiresolution

In this article, we adopted the notations for representing multiresolution operations used by Samavati et al. in [28]. The superscripts k and l used in this section represent the levels of resolution. Multiresolution operations are specified in terms of analysis filter matrices $\mathbf{A}^k$ and $\mathbf{B}^k$ and synthesis filter matrices $\mathbf{P}^k$ and $\mathbf{Q}^k$. Given a column vector of samples C^k, a lower-resolution sample vector C^{k-1} is obtained by the application of a downsampling filter on C^k. This can be expressed by the matrix equation

$$C^{k-1} = \mathbf{A}^k C^k.$$

The *details* D^{k-1}, lost after downsampling, are captured using $\mathbf{B}^k$ as follows:

$$D^{k-1} = \mathbf{B}^k C^k.$$

This process of obtaining the low-resolution sample vector C^{k-1} and the corresponding details D^{k-1} from a given high-resolution sample vector C^k is known as *decomposition*. Note that the sequences of samples along each dimension of an image can be treated independently during decomposition. Therefore, any such sequence of samples can form the column vector of samples C^k for decomposition.

The process of recovering the original high-resolution sample vector C^k from the previously obtained low-resolution sample vector C^{k-1} and the corresponding details D^{k-1} is known as *reconstruction*. The reconstruction process requires the refinement of the low-resolution sample vector C^{k-1} and the corresponding details D^{k-1} by the application of synthesis filters $\mathbf{P}^k$ and $\mathbf{Q}^k$ as follows:

$$C^k = \mathbf{P}^k C^{k-1} + \mathbf{Q}^k D^{k-1}.$$

This equation reverses the prior application of $\mathbf{A}^k$ and $\mathbf{B}^k$ on the given high-resolution sample vector C^k. Therefore, decomposition and reconstruction are inverse processes satisfying

$$\begin{bmatrix} \mathbf{A}^k \\ \mathbf{B}^k \end{bmatrix} \begin{bmatrix} \mathbf{P}^k & \mathbf{Q}^k \end{bmatrix} = \begin{bmatrix} \mathbf{I} & \mathbf{0} \\ \mathbf{0} & \mathbf{I} \end{bmatrix}.$$

If we recursively decompose a high-resolution sample vector C^k into its coarser approximations $C^l, C^{l+1}, \ldots, C^{k-1}$ and details $D^l, D^{l+1}, \ldots, D^{k-1}$, then the sequence $C^l, D^l, D^{l+1}, \ldots, D^{k-1}$ is known as a *wavelet transform*. Here, $l < k$ and C^l is the very coarse approximation of the dataset. Each of $C^{l+1}, \ldots, C^{k-1}, C^k$ can be reconstructed from the wavelet transform $C^l, D^l, D^{l+1}, \ldots, D^{k-1}$.

To simplify the notations for the rest of this article, we may omit the superscript k for the kth level of resolution assuming $F = C^k, C = C^{k-1}, D = D^{k-1}, \mathbf{A} = \mathbf{A}^k$, and $\mathbf{B} = \mathbf{B}^k, \mathbf{P} = \mathbf{P}^k$, and $\mathbf{Q} = \mathbf{Q}^k$. We further assume that the matrices are of appropriate size to satisfy the following equations:

$$C = \mathbf{A}F, \quad (1)$$

$$D = \mathbf{B}F, \quad (2)$$

$$F = \mathbf{P}C + \mathbf{Q}D. \quad (3)$$

For use in the rest of the article, let **a** and **b** denote the filter vectors containing the nonzero entries in a representative row of **A** and **B**, respectively. Similarly, let **p** and **q** stand for the filter vectors containing the nonzero entries in a representative column of **P** and **Q**, respectively. Furthermore, let *sizeof*(V) represent the number of elements in vector V and the widths of filter vectors **a** and **b** be represented by w_a and w_b, respectively, i.e. *sizeof*$(\mathbf{a}) = w_a$ and *sizeof*$(\mathbf{b}) = w_b$.

2.2. Symmetric and antisymmetric extensions

Fig. 3 shows three types of extensions as defined in [15]. Consider a sequence of n samples $(f_1, f_2, \ldots, f_n)$, corresponding to a column vector of samples $[f_1 \quad f_2 \quad \ldots \quad f_n]^T$, where $n \in \mathbb{N}$ and $n \geqslant 3$. Fig. 3(a), (b), and (c) show the extended sequences obtained through half-sample symmetric, whole-sample symmetric, and half-sample antisymmetric extensions, respectively, at both ends of $(f_1, f_2, \ldots, f_n)$. Whole-sample antisymmetry, not shown in Fig. 3, can be obtained by negating the samples in the extensions of Fig. 3(b). Note that the types of extensions at both ends of a sequence do not necessarily have to be the same (as used in Fig. 12, for example).

To be consistent with the coloring used in Fig. 3, from this point forward in this article, notations and figures may use red, purple, and green to denote the samples introduced by half-sample symmetric, whole-sample symmetric, and half-sample antisymmetric extensions, respectively.

3. Problem definition

Given a set of regular multiresolution filters in the form of symmetric/antisymmetric filter vectors $\mathbf{a}, \mathbf{b}, \mathbf{p}$, and $\mathbf{q}$, devise a balanced multiresolution scheme applicable to a high-resolution column vector of samples F that satisfies:

(i) $C = \mathbf{A}F'$ and $D = \mathbf{B}F'$, analogous to Eqs. (1) and (2), where $F \to F'$ through symmetric extensions at its boundaries and the nonzero entries in each row of **A** and **B** correspond to the regular filters in the given filter vectors **a** and **b**, respectively;
(ii) *sizeof*(C) = *sizeof*(D) i.e. a balanced decomposition;
(iii) *sizeof*(C) + *sizeof*(D) = *sizeof*(F) i.e. a compact representation of the resulting balanced wavelet transform; and
(iv) $F = \mathbf{P}C' + \mathbf{Q}D'$, analogous to Eq. (3), where $C \to C'$ and $D \to D'$ through symmetric/antisymmetric extensions at their boundaries and the nonzero entries in each column of **P** and **Q** correspond to the regular filters in the given filter vectors **p** and **q**, respectively.

4. Related work

In the next three subsections, we review the existing related work within the following three categories: multiresolution, symmetric and antisymmetric extensions, and focus+context visualization.

4.1. Multiresolution

4.1.1. Regular meshes

Here we review the multiresolution methods applicable to curves and tensor-product meshes (surfaces and

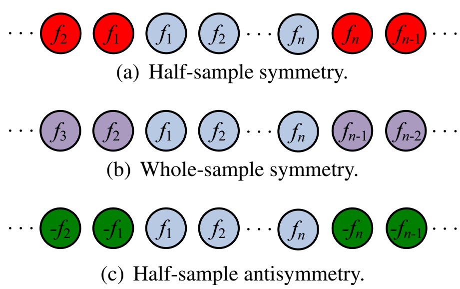

Fig. 3. Symmetric and antisymmetric extensions.

volumes) given their applicability to multidimensional images due to their regular structure.

Hierarchical representation of multiresolution tensor-product surfaces was made possible due to the pioneering work of Forsey and Bartels [10]. They localized the editing effect in a desired manner on tensor-product surfaces through hierarchically controlled subdivisions. This was done by adding finer sets of B-splines onto existing coarse sets. However, it resulted in an over-representation because the union of the sets of basis functions from different resolutions did not form a set of basis functions. Adding complementary basis functions to the coarse set of basis functions is a possible way to resolve the problem of over-representation. This means of supporting multiresolution is closely aligned to the wavelet theory approach to multiresolution [29]. Wavelet representations of details may, however, introduce undesired undulations, as pointed out by Gortler and Cohen [11]. Furthermore, under this approach, optimizing the behavior of the analysis (decomposition) using least squares is difficult due to the need to support interactive mesh manipulations [36].

Samavati and Bartels pioneered in their work on a mathematically clean and efficient approach to multiresolution based on reverse subdivision [26,3,2,4]. Under this approach, during the analysis, each coarse vertex is obtained by efficiently solving a local least squares optimization problem. The use of least squares optimization reduces the undesired undulations. Additionally, the resulting wavelets provide a much more compact support compared to the conventional wavelets for curves and regular surfaces. Some of the examples demonstrating the application of our proposed method use multiresolution filters resulting from this approach (see the examples in Section 5, for instance).

4.1.2. Images

Notable existing approaches obtaining a multiresolution representation supporting context-aware visualization of 3D images include the wavelet tree [34], segmentation of texture-space into an octree [17,24,23], octree-based tensor approximation hierarchy [30], and trilinear resampling on the Graphics Processing Unit (GPU) coupled with the deformation of regularly partitioned image regions [35]. For 4D images, the wavelet-based time–space partitioning (WTSP) tree was used in [34]. In [34], Haar [12,29] and Daubechies's D4 [7] wavelets were used to construct the wavelet transforms in each node of the wavelet and WTSP trees.

4.2. Symmetric and antisymmetric extensions

As mentioned earlier, we achieve balanced decomposition and subsequent perfect reconstruction based on the use of an appropriate combination of symmetric and antisymmetric extensions near the image and detail boundaries. In the literature, symmetric and antisymmetric extensions were used in the context of various types of wavelet transforms [18,16,1,19]. In contrast, our proposed method allows the construction of a *balanced wavelet transform*.

For end point and boundary interpolations, extraordinary filters (as opposed to regular filters) are used in multiresolution methods for curves and regular meshes, respectively. However, the use of extraordinary filters at image boundaries for boundary interpolation assigns incongruous importance to the image boundaries. So for 2D or 3D image decomposition, the general practice is to use symmetric extensions near the image boundaries to avoid boundary case evaluations using extraordinary filters [28]. However, an arbitrary choice of symmetric extension for decomposition while using a given set of multiresolution filters may eventually lead to the use of extraordinary boundary filters for a perfect reconstruction (see Section 7, for example). This can also make on-demand reconstruction of image parts corresponding to a ROI computationally untidy near the image boundaries. Therefore, a careful setup of symmetric/antisymmetric extensions for both decomposition and reconstruction is required, which can be obtained by our presented method.

4.3. Focus+context visualization

Because we chose to demonstrate the use of a balanced multiresolution scheme resulting from our method in a real-time focus+context visualization application, here we review some of the notable related work.

In many visualization tasks, it is useful to simultaneously visualize both the local and global views of the data, *possibly at different scales*, which is known as focus+context visualization. One approach to implement focus+context is to use the metaphor of lenses [33,35,13]. This metaphor is inspired by techniques used in traditional medical (see Fig. 4), technical, and scientific illustrations [14].

Our implemented approach to focus+context visualization of multidimensional images is closest to the technique presented by Taerum et al. for the visualization of small-scale clinical volumetric datasets [33]. In their approach, the resolution of a given 3D image is reduced by one level using reverse subdivision [26,3], which is rendered during user interactions to achieve interactive frame rates. The 3D image is rendered in the original resolution while there is no user-interaction. The ROI identified by a query window is enlarged by the application of B-spline subdivision to allow different levels of smoothness. Therefore, the authors used only three different levels of resolution. In contrast, our implementation for multiresolution visualization of images provides a true multiresolution framework, where the resolutions of both the coarse image (providing context information) and the enlarged ROI (providing focus information) can be controlled by the user.

5. Methodology: balanced multiresolution

In this section, we explain and demonstrate by examples how our method achieves balanced decomposition and subsequent perfect reconstruction by choosing an appropriate combination of symmetric and antisymmetric extensions near the image and detail boundaries.

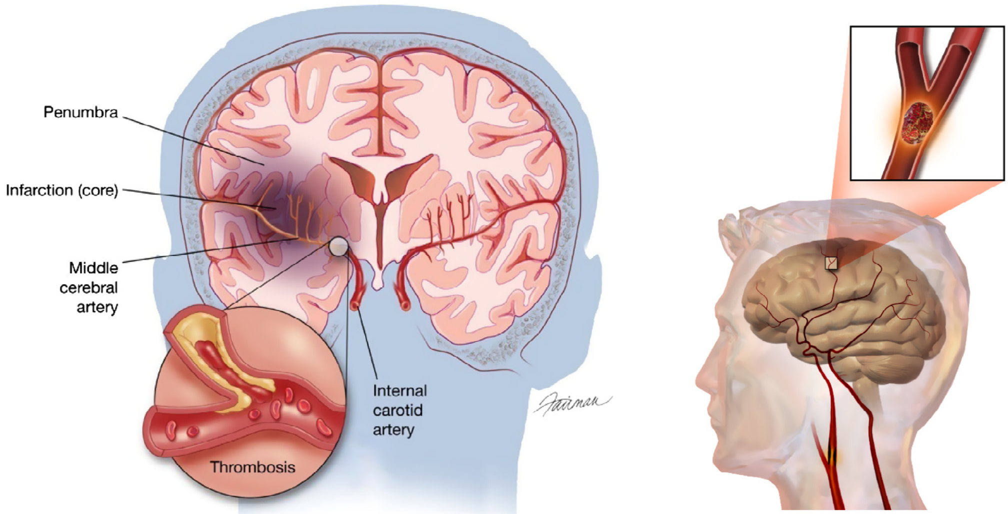

(a) A circular ROI.

(b) A rectangular ROI.

Fig. 4. Traditional focus+context visualization in medical illustrations. (a) Thrombosis in human brain. Copyright Fairman Studios, LLC. Used with permission. (b) An embolic stroke, showing a blockage lodged in a blood vessel. Blausen Medical Communications, Inc. Used under the Creative Commons Attribution 3.0 Unported license.

5.1. Balanced decomposition

We defined balanced decomposition as the task of decomposing a high-resolution image into a low-resolution image and corresponding details of equal size. Balanced decomposition of a 3D image of dimensions $2w \times 2h \times 2s$ results in an image of dimensions $w \times h \times s$ after one level of widthwise, heightwise, and depthwise decomposition. To allow l levels of balanced decomposition, we need the following conditions to be satisfied: $2w = 2^l m, 2h = 2^l n,$ and $2s = 2^l z,$ where $m, n, z \in \mathbb{Z}^+$. Disregarding the third dimension infers the same idea for a 2D image. Once the ideal dimensions are known, the high-resolution image should be uniformly resampled to those dimensions before the application of our balanced decomposition procedure.

Given the decomposition filter vectors **a** and **b**, to achieve a balanced decomposition of a column vector containing an even number of fine samples F, we first decide on the type of symmetric extension to use for decomposition based on the parity of w_a and w_b. Then an extended column vector of fine samples F' is obtained from F, through the chosen type of symmetric extension, such that $sizeof(F')$ ensures the generation of $sizeof(F)/2$ coarse samples and $sizeof(F)/2$ detail samples by a subsequent application of filter vectors **a** and **b** on F', respectively.

5.1.1. Demonstration by example

Before we outline the general construction for the balanced decomposition process, here we demonstrate how it works for a given set of decomposition filter vectors. In this example, we consider the decomposition filter vectors **a** and **b** from following set of local regular multiresolution filters [27,28]:

$$\begin{cases} \mathbf{a} &= \begin{bmatrix} -\frac{1}{4} & \frac{3}{4} & \frac{3}{4} & -\frac{1}{4} \end{bmatrix}, \\ \mathbf{b} &= \begin{bmatrix} \frac{1}{4} & -\frac{3}{4} & \frac{3}{4} & -\frac{1}{4} \end{bmatrix}, \\ \mathbf{p} &= \begin{bmatrix} \frac{1}{4} & \frac{3}{4} & \frac{3}{4} & \frac{1}{4} \end{bmatrix}, \\ \mathbf{q} &= \begin{bmatrix} -\frac{1}{4} & -\frac{3}{4} & \frac{3}{4} & \frac{1}{4} \end{bmatrix}. \end{cases} \tag{4}$$

The filter vectors in Eq. (4) are known as the *short* filters of quadratic (third order) B-spline [28] and were constructed by reversing Chaikin subdivision [6]. Recall from Section 2 that filter vectors **a** and **b** contain the nonzero entries in a representative row of analysis filter matrices **A** and **B**, respectively.

For the purpose of demonstration, assume that we are given a fine column vector of 8 samples $F = [f_1 \quad f_2 \quad \ldots \quad f_8]^T$, on which we have to perform a balanced decomposition. Provided $sizeof(F) = 8$, a balanced decomposition should result in column vectors of coarse samples $C = [c_1 \quad c_2 \quad c_3 \quad c_4]^T$ and detail samples $D = [d_1 \quad d_2 \quad d_3 \quad d_4]^T$.

In Fig. 5, we present one possible setup to obtain such a balanced decomposition. It shows the application of equations $C = \mathbf{A}F'$ and $D = \mathbf{B}F'$, analogous to Eqs. (1) and (2), where $F' = [f_1 \quad f_1 \quad f_2 \quad \ldots \quad f_8 \quad f_8]^T$. First, note that F' was obtained by extending the given sample vector F by 2 extra samples. In general, when the dilation factor is 2, a given column vector of fine samples F, with $sizeof(F) = 2n$ for $n \in \mathbb{Z}^+$, does not have enough samples to accommodate n shifts of both **a** and **b** for generating n coarse and n detail samples, respectively. The number of extra samples x, required for a balanced decomposition can be obtained by the general formula:

$$x = max(w_a, w_b) + 2(n-1) - 2n \tag{5}$$

$$\Rightarrow x = max(w_a, w_b) - 2. \tag{6}$$

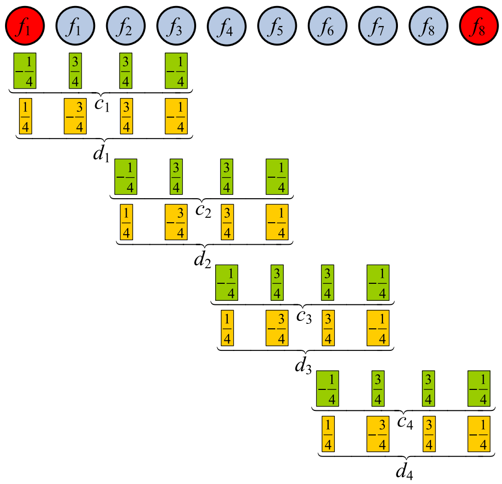

Fig. 5. Balanced decomposition of 8 fine samples using the decomposition filter vectors **a** and **b** from Eq. (4).

Here we explain how Eq. (5) evaluates x. We need at least $max(w_a, w_b)$ fine samples to obtain both c_1 and d_1, which explains the first term on the right-hand side of Eq. (5). Next, because the dilation factor is 2, every 2 additional samples will guarantee the generation of an additional pair of c_i and d_i. Here, $i \in \{2, \ldots, n\}$ because we want to generate $|\{2, \ldots, n\}| = n - 1$ more coarse samples and $n - 1$ more detail samples to achieve a balanced decomposition. This indicates the need for an additional $2(n - 1)$ fine samples, justifying the addition of the second term on the right-hand side of Eq. (5). Therefore, subtracting $2n$ i.e. the $sizeof(F)$ in the third term gives us the required number of extra samples.

For the families of multiresolution filters we consider in this article, w_a and w_b are either both even or both odd. For example, see the decomposition filter vectors obtained from B-spline wavelets [28], biorthogonal and reverse biorthogonal wavelets [5,8], and Meyer wavelets [21,8]. The multiresolution filter vectors obtained from most such wavelets and their scaling functions are available in commonly used mathematical software packages such as MATLAB [20]. For the given filter vectors **a** and **b** in Eq. (4), because both w_a and w_b are even, observe that the extension of F by 2 extra samples to obtain F' was achieved by half-sample symmetric extension at both ends of F. Here we would have used whole-sample symmetric extension instead if both w_a and w_b were odd. Use of an appropriate type of symmetric extension is required to avoid the use of any extraordinary boundary filters for a perfect reconstruction. We justify our choice of symmetric extension for a balanced decomposition later in Section 5.3.

Finally, as shown in Fig. 5, the filter vectors **a** and **b** in Eq. (4) are applied to the samples in F' to obtain C and D in order to complete the balanced decomposition process. For instance, the coarse sample c_1 and the detail sample d_1 are computed from the first 4 samples in F' as follows:

$$\begin{cases} c_1 &= -\frac{1}{4}f_1 + \frac{3}{4}f_1 + \frac{3}{4}f_2 - \frac{1}{4}f_3, \\ d_1 &= \frac{1}{4}f_1 - \frac{3}{4}f_1 + \frac{3}{4}f_2 - \frac{1}{4}f_3. \end{cases} \tag{7}$$

Note that the total contribution of f_1 in the construction of c_1 is $\frac{1}{2}f_1$, written as $-\frac{1}{4}f_1 + \frac{3}{4}f_1$ in Eq. (7) through an implicit sample split operation. A similar sample split is observed in the construction of d_1, as shown in Eq. (7). Therefore, the symmetric extensions at both ends of F implicitly lead to a number of sample split operations during decomposition.

Therefore, for $n \in \mathbb{Z}^+$, a balanced multiresolution scheme based on the *short* filters of quadratic B-spline given in Eq. (4) can make use of the matrix equations

$$\begin{bmatrix} c_1 \\ c_2 \\ \vdots \\ c_n \end{bmatrix} = \begin{bmatrix} -\frac{1}{4} & \frac{3}{4} & \frac{3}{4} & -\frac{1}{4} & 0 & 0 & 0 & \cdots \\ 0 & 0 & -\frac{1}{4} & \frac{3}{4} & \frac{3}{4} & -\frac{1}{4} & 0 & \cdots \\ \vdots & \vdots & \vdots & \vdots & \vdots & \vdots & \vdots & \ddots \end{bmatrix} \begin{bmatrix} f_1 \\ f_1 \\ f_2 \\ \vdots \\ f_{2n-1} \\ f_{2n} \\ f_{2n} \end{bmatrix}$$

and

$$\begin{bmatrix} d_1 \\ d_2 \\ \vdots \\ d_n \end{bmatrix} = \begin{bmatrix} \frac{1}{4} & -\frac{3}{4} & \frac{3}{4} & -\frac{1}{4} & 0 & 0 & 0 & \cdots \\ 0 & 0 & \frac{1}{4} & -\frac{3}{4} & \frac{3}{4} & -\frac{1}{4} & 0 & \cdots \\ \vdots & \vdots & \vdots & \vdots & \vdots & \vdots & \vdots & \ddots \end{bmatrix} \begin{bmatrix} f_1 \\ f_1 \\ f_2 \\ \vdots \\ f_{2n-1} \\ f_{2n} \\ f_{2n} \end{bmatrix}$$

for the decomposition process, analogous to Eqs. (1) and (2).

5.1.2. General construction

Now we present our general approach for achieving a balanced decomposition. Given the symmetric/antisymmetric decomposition filter vectors **a** and **b** containing only regular filters, carry out the following steps to achieve a balanced decomposition of a fine column vector of samples F, where $sizeof(F) = 2n$ for a suitably large $n \in \mathbb{Z}^+$.

1. Determine x, the number of extra samples required for a balanced decomposition using Eq. (6).
2. If both w_a and w_a are even, extend F with x extra samples using half-sample symmetric extension to obtain F'. Use whole-sample symmetric extension instead if both w_a and w_a are odd. Justification of our choice of symmetric extension can be found in Section 5.3. To avoid giving inconsistent importance to any end (boundary) of F:
   (a) If x is even, introduce $x/2$ samples at each end of F.
   (b) If x is odd, introduce $\lfloor x/2 \rfloor$ samples at one end and $\lfloor x/2 \rfloor + 1$ samples at the other end of F. Let us refer to the end at which $\lfloor x/2 \rfloor + 1$ samples are introduced as the *odd end*. Alternate between the ends of F as the choice of the odd end during multiple levels of decomposition.
3. To obtain C and D such that $sizeof(C) = sizeof(D)$, use equations $C = \mathbf{A}F'$ and $D = \mathbf{B}F'$, analogous to Eqs. (1) and (2).

5.2. Perfect reconstruction

Given the reconstruction filter vectors **p** and **q** that can reverse the application of the decomposition filter vectors **a** and **b**, to achieve a perfect reconstruction of the column vector of fine samples F from its prior balanced decomposition into C and D, we first reconstruct as many interior samples of F as possible by the application of **p** and **q** on C and D, using Eq. (3). To evaluate the samples near each boundary (end) of F, we form a square system of linear equations based on the prior construction of corresponding boundary samples in C and D, where the unknowns constitute the boundary samples of F yet to be reconstructed. Symbolically solving two such square systems for the two boundaries of F reveals the extended versions of C and D (denoted by C' and D', respectively) required for a perfect reconstruction by the application of **p** and **q** using equation $F = \mathbf{P}C' + \mathbf{Q}D'$, analogous to Eq. (3).

5.2.1. Demonstration by example

Here we demonstrate how we perform a perfect reconstruction of F following its balanced decomposition to C and D by means of an example, before giving the general construction for our perfect reconstruction process. In this example, we consider the reconstruction filter vectors **p** and **q** given in Eq. (4). Recall from Section 2 that filter vectors **p** and **q** contain the nonzero entries in a representative column of synthesis filter matrices **P** and **Q**, respectively. This example to demonstrate our perfect reconstruction process is an extension of the example shown in Fig. 5. So, from the resulting column vectors coarse samples $C = [c_1 \quad c_2 \quad c_3 \quad c_4]^T$ and detail samples $D = [d_1 \quad d_2 \quad d_3 d_4]^T$ in Section 5.1, we now want to reconstruct the corresponding column vector of fine samples $F = [f_1 \quad f_2 \quad \dots \quad f_8]^T$.

In Fig. 6, we show the application of the filter vectors **p** and **q** to the samples in C and D, respectively. For instance, the fine sample f_2 is reconstructed from the first two coarse samples and the first two detail samples as follows:

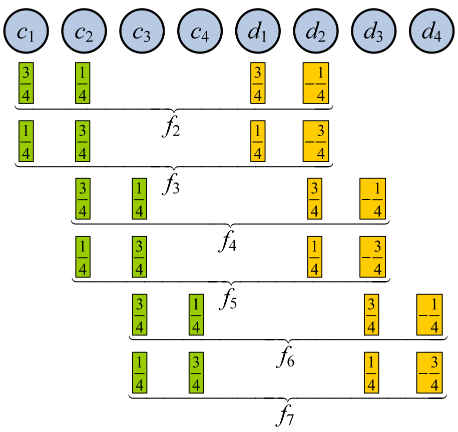

Fig. 6. Perfect reconstruction of 6 of the 8 fine samples using the reconstruction filter vectors **p** and **q** from Eq. (4).

$$f_2 = \frac{3}{4}c_1 + \frac{1}{4}c_2 + \frac{3}{4}d_1 - \frac{1}{4}d_2.$$

Note that the application of the filter vectors **p** and **q** to the samples in C and D in Fig. 6 left two samples, f_1 and f_8, near the two ends of F not reconstructed. Note that having two samples near the boundaries of F yet to reconstruct is specific to this example. The example in Section 5.4 receives 5 samples yet to reconstruct at this stage. Now, to reconstruct f_1, we form the following 1×1 system of linear equations based on the prior construction of c_1 (as shown in Fig. 5) to which f_1 made some contribution during decomposition:

$$\begin{aligned} c_1 &= -\frac{1}{4}f_1 + \frac{3}{4}f_1 + \frac{3}{4}f_2 - \frac{1}{4}f_3 \qquad (8)\\ \Rightarrow f_1 &= 2c_1 - \frac{3}{2}f_2 + \frac{1}{2}f_3\\ \Rightarrow f_1 &= 2c_1 - \frac{3}{2}\left(\frac{3}{4}c_1 + \frac{1}{4}c_2 + \frac{3}{4}d_1 - \frac{1}{4}d_2\right)\\ &\quad + \frac{1}{2}\left(\frac{1}{4}c_1 + \frac{3}{4}c_2 + \frac{1}{4}d_1 - \frac{3}{4}d_2\right)\\ \Rightarrow f_1 &= c_1 - d_1. \qquad (9) \end{aligned}$$

Although it appears from Eq. (9) that f_1 is not reconstructed using *regular filters*, our prior appropriate choice of symmetric extension to obtain F' from F (justified later in Section 5.3) guarantees that we can rewrite f_1 using the regular filter values from **p** and **q** in Eq. (4). This is achieved by a rearrangement of the right-hand side of Eq. (9), which is implicitly equivalent to performing two sample split operations:

$$f_1 = \frac{1}{4}c_1 + \frac{3}{4}c_1 + \frac{1}{4}(-d_1) - \frac{3}{4}d_1. \qquad (10)$$

This rewriting step is important because it allows the reconstruction of fine samples near the boundaries of F without the use of any extraordinary boundary filters. Eq. (10) now yields the introduction of one extra coarse sample through half-sample symmetric extension and one extra detail sample through half-sample antisymmetric extension for the reconstruction of f_1, as shown in Fig. 7. We use a similar approach to determine how to reconstruct the boundary sample f_8, resulting in

$$f_8 = \frac{3}{4}c_4 + \frac{1}{4}c_4 + \frac{3}{4}d_1 - \frac{1}{4}(-d_4), \qquad (11)$$

as reflected in Fig. 7. This concludes the perfect reconstruction process.

Therefore, based on our findings from Eqs. (10) and (11), for a given column vector of $2n$ fine samples for a suitably large $n \in \mathbb{Z}^+$, we get

$$\begin{cases} f_1 &= \frac{1}{4}c_1 + \frac{3}{4}c_1 + \frac{1}{4}(-d_1) - \frac{3}{4}d_1,\\ f_{2n} &= \frac{3}{4}c_n + \frac{1}{4}c_n + \frac{3}{4}d_n - \frac{1}{4}(-d_n). \end{cases}$$

So a balanced multiresolution scheme based on the *short* filters of quadratic B-spline given in Eq. (4) will make use of the matrix equation

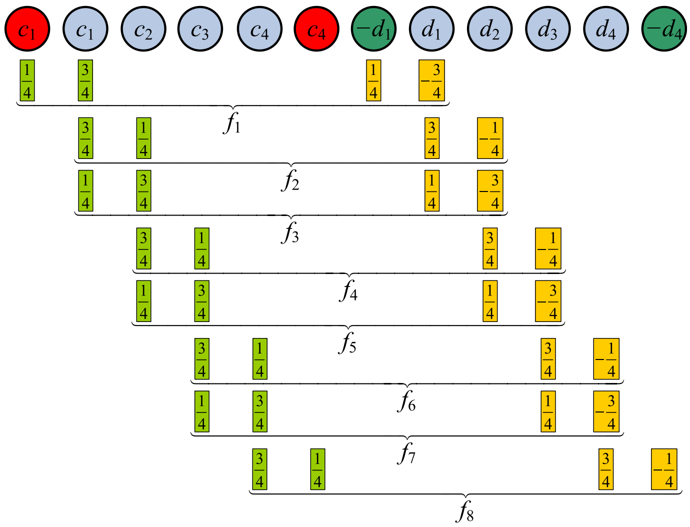

Fig. 7. Perfect reconstruction of 8 fine samples using the reconstruction filter vectors **p** and **q** from Eq. (4).

$$\begin{bmatrix} f_1 \\ f_2 \\ \vdots \\ f_{2n} \end{bmatrix} = \begin{bmatrix} \frac{1}{4} & \frac{3}{4} & 0 & 0 & \cdots & 0 & 0 & 0 \\ 0 & \frac{3}{4} & \frac{1}{4} & 0 & \cdots & 0 & 0 & 0 \\ 0 & \frac{1}{4} & \frac{3}{4} & 0 & \cdots & 0 & 0 & 0 \\ 0 & 0 & \frac{3}{4} & \frac{1}{4} & \cdots & 0 & 0 & 0 \\ 0 & 0 & \frac{1}{4} & \frac{3}{4} & \cdots & 0 & 0 & 0 \\ \vdots & \vdots & \vdots & \vdots & \ddots & \vdots & \vdots & \vdots \\ 0 & 0 & 0 & 0 & \cdots & \frac{3}{4} & \frac{1}{4} & 0 \\ 0 & 0 & 0 & 0 & \cdots & \frac{1}{4} & \frac{3}{4} & 0 \\ 0 & 0 & 0 & 0 & \cdots & 0 & \frac{3}{4} & \frac{1}{4} \end{bmatrix} \begin{bmatrix} c_1 \\ c_1 \\ c_2 \\ \vdots \\ c_n \\ c_n \end{bmatrix} + \begin{bmatrix} \frac{1}{4} & -\frac{3}{4} & 0 & 0 & \cdots & 0 & 0 & 0 \\ 0 & \frac{3}{4} & -\frac{1}{4} & 0 & \cdots & 0 & 0 & 0 \\ 0 & \frac{1}{4} & -\frac{3}{4} & 0 & \cdots & 0 & 0 & 0 \\ 0 & 0 & \frac{3}{4} & -\frac{1}{4} & \cdots & 0 & 0 & 0 \\ 0 & 0 & \frac{1}{4} & -\frac{3}{4} & \cdots & 0 & 0 & 0 \\ \vdots & \vdots & \vdots & \vdots & \ddots & \vdots & \vdots & \vdots \\ 0 & 0 & 0 & 0 & \cdots & \frac{3}{4} & -\frac{1}{4} & 0 \\ 0 & 0 & 0 & 0 & \cdots & \frac{1}{4} & -\frac{3}{4} & 0 \\ 0 & 0 & 0 & 0 & \cdots & 0 & \frac{3}{4} & -\frac{1}{4} \end{bmatrix} \begin{bmatrix} -d_1 \\ d_1 \\ d_2 \\ \vdots \\ d_n \\ -d_n \end{bmatrix}$$

for the reconstruction process, analogous to Eq. (3).

5.2.2. General construction

Now we describe our general approach to achieve perfect reconstruction. Given the symmetric/antisymmetric reconstruction filter vectors **p** and **q** containing only regular filters that can reverse the application of the decomposition filter vectors **a** and **b**, carry out the following steps to perfectly reconstruct the column vector of fine samples F from its prior balanced decomposition into C and D.

1. Assume that $F = \left[F_l^T \;\; F_m^T \;\; F_r^T\right]^T$, where F_l and F_r respectively contain some samples at the left and right boundaries of F, and F_m contains the remaining interior samples of F. To reconstruct the samples in F_m, use the equation $F_m = \mathbf{P}C + \mathbf{Q}D$, analogous to Eq. (3). The samples in F_l and F_r are yet to be reconstructed.
   (In the example above, we had $F_l = [f_1], F_m = [f_2 \;\; f_3 \;\; \ldots \;\; f_7]^T$, and $F_r = [f_8]$. Note that F_l and F_r may contain more samples; for instance, the F_l and F_r encountered in 5.4 have 2 and 3 samples, respectively.)
2. To reconstruct the samples in F_l:
   (a) Form a system of linear equations based on the prior construction of some coarse and detail boundary samples, to which the fine samples in F_l made some contributions during the decomposition process. It should be a $q \times q$ system, where $q = sizeof(F_l)$ and the unknowns are the samples of F_l.
   (For example, see the 1×1 system formed by Eq. (8) and the 2×2 system formed by the two equations in (19).)
   (b) Solving the system formed in step 2(a) symbolically will evaluate the samples in F_l as a linear combination of some samples from C and D.
   (For example, see Eq. (9) and the two equations in (20).)
   (c) Rewrite the linear combination(s) of coarse and detail samples on the right-hand side(s) of the equation(s) obtained in step 2(b) using the regular filter values from the filter vectors **p** and **q** as coefficients. Such rewriting of fine samples here correlates to performing sample split operations. This will reveal the following two pieces of information applicable to the left boundaries of C and D for a perfect reconstruction: (i) the type of symmetric/antisymmetric extension that must be used and

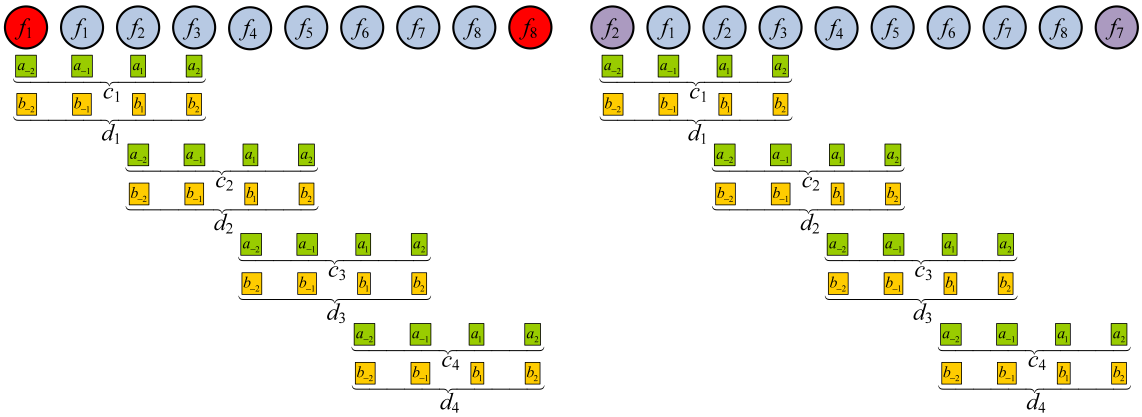

(a) Balanced decomposition using half-sample symmetric extension.

(b) Balanced decomposition using whole-sample symmetric extension.

Fig. 8. Balanced decomposition of 8 fine samples using the decomposition filter vectors **a** and **b** from Eq. (12).

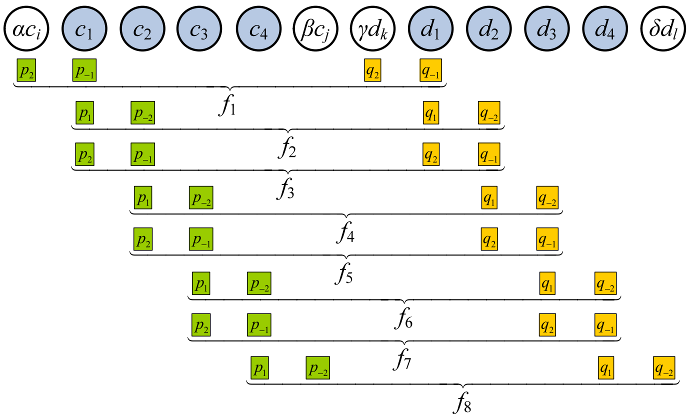

Fig. 9. Perfect reconstruction of 8 fine samples using the reconstruction filter vectors **p** and **q** from Eq. (12).

(ii) the number of extra samples that must be to introduced.(For example, see Eq. (10) and the equations in (21).)

3. Use an approach similar to that in step 2 to reconstruct the samples in F_r.

Note that steps 2–3 above allow the generation of C' and D' respectively from C and D, such that condition (iv) of the problem definition given in Section 3 is satisfied.

5.3. Choice of symmetric extension for decomposition

5.3.1. Claim

For a given set of symmetric/antisymmetric multiresolution filter vectors $\mathbf{a}, \mathbf{b}, \mathbf{p}$, and $\mathbf{q}$, even values of w_a and w_b imply the use of half-sample symmetric extensions at the image boundaries during a balanced decomposition to ensure a perfect reconstruction only using the regular reconstruction filters from $\mathbf{p}$ and $\mathbf{q}$. On the other hand, odd values of w_a and w_b imply the use of whole-sample symmetric extensions instead.

5.3.2. Proof outline

We outline the proof by means of an example that makes use of the filter vectors containing only regular filters,

$$\begin{cases} \mathbf{a} &= [a_{-2} \quad a_{-1} \quad a_1 \quad a_2], \\ \mathbf{b} &= [b_{-2} \quad b_{-1} \quad b_1 \quad b_2], \\ \mathbf{p} &= [p_{-2} \quad p_{-1} \quad p_1 \quad p_2], \\ \mathbf{q} &= [q_{-2} \quad q_{-1} \quad q_1 \quad q_2]. \end{cases} \tag{12}$$

The widths of the filter vectors $\mathbf{a}, \mathbf{b}, \mathbf{p}$, and $\mathbf{q}$ in Eq. (12) are assumed to be 4 as in the case of the filter vectors containing the *short* filters of quadratic B-spline in Eq. (4). So, here w_a and w_b are even. Next, two possible balanced decompositions of a fine column vector of 8 samples $F = [f_1 \quad f_2 \quad \dots \quad f_8]^T$ are shown by the use of half-sample and whole-sample symmetric extensions at its boundaries in Figs. 8(a) and (b), respectively.

Now, our goal is to perfectly reconstruct F from the column vectors of coarse samples $C = [c_1 \quad c_2 \quad c_3 \quad c_4]^T$ and detail samples $D = [d_1 \quad d_2 \quad d_3 \quad d_4]^T$ using only the regular reconstruction filters vectors **p** and **q** from Eq. (12) as shown in Fig. 9.

We intend to evaluate the unknowns in Fig. 9, which are $\alpha c_i \in \{-c_1, c_1, -c_2, c_2\}, \beta c_j \in \{-c_3, c_3, -c_4, c_4\}, \gamma d_k \in \{-d_1, d_1, -d_2, d_2\}$, and $\delta d_l \in \{-d_3, d_3, -d_4, d_4\}$ near the boundaries of C and D. Once evaluated, these will reveal the type of symmetric/antisymmetric extensions to be used at the boundaries of C and D to ensure a perfect reconstruction using only the regular reconstruction filters. Here $\alpha, \beta, \gamma, \delta \in \{+, -\}$ represent the signs of c_i, c_j, d_k and d_l, respectively. When negative, they allow the representation of antisymmetric extensions.

Now, let us try to evaluate αc_i. As shown in Fig. 9, αc_i contributes to the reconstruction of f_1. If we consider the balanced decomposition shown in Fig. 8(a) and try to evaluate f_1 following our general approach from Section 5.2, we get

$$\begin{aligned} c_1 &= a_{-2} f_1 + a_{-1} f_1 + a_1 f_2 + a_2 f_3 \\ \Rightarrow f_1 &= \frac{1}{a_{-2}+a_{-1}} c_1 - \frac{a_1}{a_{-2}+a_{-1}} f_2 - \frac{a_2}{a_{-2}+a_{-1}} f_3 \\ \Rightarrow f_1 &= \frac{1}{a_{-2}+a_{-1}} c_1 \\ &\quad - \frac{a_1}{a_{-2}+a_{-1}} (p_1 c_1 + p_{-2} c_2 + q_1 d_1 + q_{-2} d_2) \\ &\quad - \frac{a_2}{a_{-2}+a_{-1}} (p_2 c_1 + p_{-1} c_2 + q_2 d_1 + q_{-1} d_2) \\ \Rightarrow f_1 &= \left(\frac{1 - a_1 p_1 - a_2 p_2}{a_{-2}+a_{-1}} \right) c_1 + \left(\frac{-a_1 p_{-2} - a_2 p_{-1}}{a_{-2}+a_{-1}} \right) c_2 \\ &\quad + \left(\frac{-a_1 q_1 - a_2 q_2}{a_{-2}+a_{-1}} \right) d_1 + \left(\frac{-a_1 q_{-2} - a_2 q_{-1}}{a_{-2}+a_{-1}} \right) d_2. \end{aligned} \tag{13}$$

Next, if we consider the balanced decomposition shown in Fig. 8(b) and try to evaluate f_1 following our general approach from Section 5.2, we get

$$\begin{aligned} c_1 &= a_{-2} f_2 + a_{-1} f_1 + a_1 f_2 + a_2 f_3 \\ \Rightarrow f_1 &= \frac{1}{a_{-1}} c_1 - \frac{a_{-2}+a_1}{a_{-1}} f_2 - \frac{a_2}{a_{-1}} f_3 \\ \Rightarrow f_1 &= \frac{1}{a_{-1}} c_1 - \frac{a_{-2}+a_1}{a_{-1}} (p_1 c_1 + p_{-2} c_2 + q_1 d_1 + q_{-2} d_2) \\ &\quad + \frac{a_2}{a_{-1}} (p_2 c_1 + p_{-1} c_2 + q_2 d_1 + q_{-1} d_2) \\ \Rightarrow f_1 &= \left(\frac{1 - a_{-2} p_1 - a_1 p_1 - a_2 p_2}{a_{-1}} \right) c_1 \\ &\quad + \left(\frac{-a_{-2} p_2 - a_1 p_2 - a_2 p_{-1}}{a_{-1}} \right) c_2 \\ &\quad + \left(\frac{-a_{-2} q_1 - a_1 q_1 - a_2 q_2}{a_{-1}} \right) d_1 \\ &\quad + \left(\frac{-a_{-2} q_2 - a_1 q_2 - a_2 q_{-1}}{a_{-1}} \right) d_2. \end{aligned} \tag{14}$$

Let the filter values multiplied to c_1 and c_2 in the reconstruction of f_1 be denoted by $w(c_1)$ and $w(c_2)$, respectively. In Eq. (13),

$$\begin{cases} w(c_1) = \frac{1 - a_1 p_1 - a_2 p_2}{a_{-2}+a_{-1}}, \\ w(c_2) = \frac{-a_1 p_{-2} - a_2 p_{-1}}{a_{-2}+a_{-1}}, \end{cases} \tag{15}$$

which result from using half-sample symmetric extension at the left boundary F for a balanced decomposition. On the other hand, in Eq. (14),

$$\begin{cases} w(c_1) = \frac{1 - a_{-2} p_1 - a_1 p_1 - a_2 p_2}{a_{-1}}, \\ w(c_2) = \frac{-a_{-2} p_2 - a_1 p_2 - a_2 p_{-1}}{a_{-1}}, \end{cases} \tag{16}$$

which result from using whole-sample symmetric extension instead. Now, according to Fig. 9, f_1 is reconstructed as follows:

$$f_1 = p_2(\alpha c_i) + p_{-1} c_1 + q_2(\alpha d_k) - q_{-1} d_1. \tag{17}$$

If we consider $\alpha c_i = -c_1$ in Eq. (17) for example, then $w(c_1) = -p_2 + p_{-1}$ and $w(c_2) = 0$. If $-c_1$ is substituted in Fig. 9 in place of αc_i, it would then reveal the need for half-sample antisymmetric extension for the left boundary of C to be used during reconstruction. In this manner, Table 1 lists the sufficient conditions for all possible values of αc_i. Note that each possible value of αc_i yields a particular type of extension (listed in Table 1) for the left boundary of C.

Now, if we substitute the actual values of the corresponding regular filters of quadratic B-spline from Eq. (4) in Eqs. (15) and (16), we find that Eq. (15) only satisfies the sufficient conditions under case I (i.e. $\alpha c_i = c_1$) in Table 1 and Eq. (16) does not satisfy the sufficient conditions under any of the cases. Recall that Eq. (15) was obtained by the use of half-sample symmetric extension on the left boundary of F for a balanced decomposition. This implies that the use of half-sample symmetric extension at the left boundary of F for a balanced decomposition will ensure the perfect reconstruction of that boundary only using regular reconstruction filters. Similarly, for the regular filters of quadratic B-spline from Eq. (4), we can show that $\beta c_j = c_4, \gamma d_k = -d_1$, and $\delta d_l = -d_4$; and they all require the use of half-sample symmetric extension at the boundaries of F for a balanced decomposition.

In the above manner, we can show that for any set of symmetric/antisymmetric filter vectors **a**, **b**, **p**, and **q**, where w_a and w_b are even, half-sample symmetric extension can be used at the boundaries of a column vector of fine samples for a balanced decomposition to ensure a perfect reconstruction only using the regular reconstruction filters from **p** and **q**. A similar proof can be outlined to show that odd values of w_a and w_b imply the use of whole-sample symmetric extension instead.

Table 1
Sufficient conditions for symmetric and antisymmetric extensions.

Case	Sufficient conditions	αc_i	Type of extension
I	$\begin{cases} w(c_1) = p_2 + p_{-1} \\ w(c_2) = 0 \end{cases}$	c_1	Half-sample symmetry
II	$\begin{cases} w(c_1) = -p_2 + p_{-1} \\ w(c_2) = 0 \end{cases}$	$-c_1$	Half-sample antisymmetry
III	$\begin{cases} w(c_1) = p_{-1} \\ w(c_2) = p_2 \end{cases}$	c_2	Whole-sample symmetry
IV	$\begin{cases} w(c_1) = p_{-1} \\ w(c_2) = -p_2 \end{cases}$	$-c_2$	Whole-sample antisymmetry

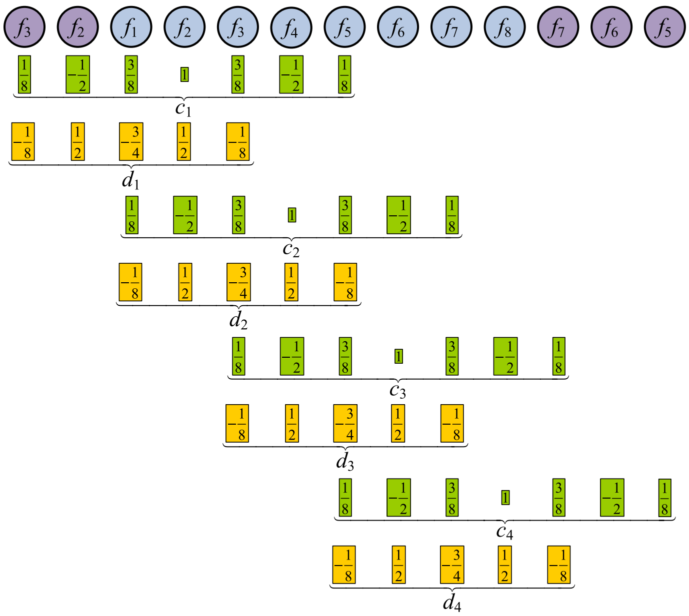

Fig. 10. Balanced decomposition of 8 fine samples using the decomposition filter vectors **a** and **b** from Eq. (18).

5.4. Further demonstration by example

The example in this section illustrates the use of decomposition filter vectors of odd width for a balanced decomposition as opposed to the even width of decomposition filter vectors in the previous example (subSections 5.1 and 5.2). Further examples are provided in Appendix A.

5.4.1. Balanced decomposition

Here we demonstrate our general approach described in Section 5.1 using the decomposition filter vectors **a** and **b** from following set of local regular multiresolution filters [3,28]:

$$\begin{cases} \mathbf{a} &= \left[\tfrac{1}{8} \quad -\tfrac{1}{2} \quad \tfrac{3}{8} \quad 1 \quad \tfrac{3}{8} \quad -\tfrac{1}{2} \quad \tfrac{1}{8}\right], \\ \mathbf{b} &= \left[-\tfrac{1}{8} \quad \tfrac{1}{2} \quad -\tfrac{3}{4} \quad \tfrac{1}{2} \quad -\tfrac{1}{8}\right], \\ \mathbf{p} &= \left[\tfrac{1}{8} \quad \tfrac{1}{2} \quad \tfrac{3}{4} \quad \tfrac{1}{2} \quad \tfrac{1}{8}\right], \\ \mathbf{q} &= \left[\tfrac{1}{8} \quad \tfrac{1}{2} \quad \tfrac{3}{8} \quad -1 \quad \tfrac{3}{8} \quad \tfrac{1}{2} \quad \tfrac{1}{8}\right]. \end{cases} \tag{18}$$

The filter vectors in Eq. (18) are known as the *inverse powers of two* filters of cubic (fourth order) B-spline [28]. We explain the balanced decomposition process using the decomposition filter vectors in Eq. (18) through the example shown in Fig. 10. Similar to the previous example shown in Fig. 5, here we have a column vector of 8 fine samples $F = [f_1 \quad f_2 \quad \dots \quad f_8]^T$ that we want to decompose into the column vectors of coarse samples $C = [c_1 \quad c_2 \quad c_3 \quad c_4]^T$ and detail samples $D = [d_1 \quad d_2 \quad d_3 \quad d_4]^T$.

Fig. 10 shows one possible balanced decomposition using our general approach presented in Section 5.1. Step 1 of our *general construction* given in Section 5.1 reveals that 5 extra samples are required to ensure a balanced decomposition. As noted earlier, w_a and w_b for the filter vectors in Eq. (18) are odd. So according to step 2, whole-sample symmetric extension is used to introduce 2 extra samples at one end and 3 extra samples at the other end of F to obtain the extended column vector of fine samples $F' = [f_3 \quad f_2 \quad f_1 \quad f_2 \quad \dots \quad f_8 \quad f_7 \quad f_6 \quad f_5]^T$. Finally, according to step 3, the filter vectors **a** and **b** from Eq. (18) are applied to F' to obtain C and D by means of the equations $C = \mathbf{A}F'$ and $D = \mathbf{B}F'$, analogous to Eqs. (1) and (2). Therefore, for $n \in \mathbb{Z}^+$, a balanced multiresolution scheme based on the *inverse powers of two* filters of cubic B-spline given in Eq. (18) can make use of the matrix equations

$$\begin{bmatrix} c_1 \\ c_2 \\ \vdots \\ c_n \end{bmatrix} = \begin{bmatrix} \frac{1}{8} & -\frac{1}{2} & \frac{3}{8} & 1 & \frac{3}{8} & -\frac{1}{2} & \frac{1}{8} & 0 & 0 & 0 & \cdots \\ 0 & 0 & \frac{1}{8} & -\frac{1}{2} & \frac{3}{8} & 1 & \frac{3}{8} & -\frac{1}{2} & \frac{1}{8} & 0 & \cdots \\ \vdots & \vdots & \vdots & \vdots & \vdots & \vdots & \vdots & \vdots & \vdots & \vdots & \ddots \end{bmatrix} \begin{bmatrix} f_3 \\ f_2 \\ f_1 \\ f_2 \\ \vdots \\ f_{2n-1} \\ f_{2n} \\ f_{2n-1} \\ f_{2n-2} \\ f_{2n-3} \end{bmatrix}$$

and

$$\begin{bmatrix} d_1 \\ d_2 \\ \vdots \\ d_n \end{bmatrix} = \begin{bmatrix} -\frac{1}{8} & \frac{1}{2} & -\frac{3}{4} & \frac{1}{2} & -\frac{1}{8} & 0 & 0 & 0 & \cdots \\ 0 & 0 & -\frac{1}{8} & \frac{1}{2} & -\frac{3}{4} & \frac{1}{2} & -\frac{1}{8} & 0 & \cdots \\ \vdots & \vdots & \vdots & \vdots & \vdots & \vdots & \vdots & \vdots & \ddots \end{bmatrix} \begin{bmatrix} f_3 \\ f_2 \\ f_1 \\ f_2 \\ \vdots \\ f_{2n-1} \\ f_{2n} \\ f_{2n-1} \end{bmatrix}$$

for the decomposition process, analogous to Eqs. (1) and (2).

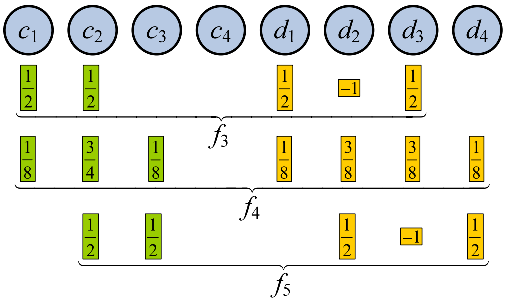

Fig. 11. Perfect reconstruction of 3 of the 8 fine samples using the reconstruction filter vectors **p** and **q** from Eq. (18).

5.4.2. Perfect reconstruction

Here we demonstrate our general approach described in Section 5.2 using the reconstruction filter vectors **p** and **q** given in Eq. (18). They can reverse the application of the decomposition filters vectors **a** and **b** from Eq. (18). Given the column vectors of coarse samples $C = [c_1 \quad c_2 \quad c_3 \quad c_4]^T$ and detail samples $D = [d_1 \quad d_2 \quad d_3 \quad d_4]^T$ (obtained as shown in Fig. 10), we now want to perfectly reconstruct the column vector fine samples $F = [f_1 \quad f_2 \quad \dots \quad f_8]^T$.

Fig. 11 shows the reconstruction of $F_m = [f_3 \quad f_4 \quad f_5]^T$ according to step 1 of our *general construction* given in Section 5.2. $F_l = [f_1 \quad f_2]^T$ and $F_r = [f_6 \quad f_7 \quad f_8]^T$ are yet to be reconstructed.

Next, following step 2(a) of our given *general construction*, we form the following system of 2 linear equations in 2 unknowns (f_1 and f_2 in F_l):

$$\begin{cases} c_1 = \frac{1}{8}f_3 - \frac{1}{2}f_2 + \frac{3}{8}f_1 + f_2 + \frac{3}{8}f_3 - \frac{1}{2}f_4 + \frac{1}{8}f_5, \\ d_1 = -\frac{1}{8}f_3 + \frac{1}{2}f_2 - \frac{3}{4}f_1 + \frac{1}{2}f_2 - \frac{1}{8}f_3. \end{cases} \tag{19}$$

The equations in (19) were obtained from Fig. 10, which shows how c_1 and d_1 were computed during decomposition. Note that in (19), we can replace f_3, f_4, and f_5 with the corresponding linear combinations of coarse and detail samples from Fig. 11. Then following step 2(b), solving the 2×2 system formed by the equations in (19) gives

$$\begin{cases} f_1 = c_1 - d_1 + d_2, \\ f_2 = \frac{7}{8}c_1 + \frac{1}{8}c_2 + \frac{3}{8}d_1 + \frac{1}{2}d_2 + \frac{1}{8}d_3. \end{cases} \tag{20}$$

Now, according to step 2(c), the equations in (20) can be rewritten as follows such that the coefficients of the coarse and detail samples are all regular filters from Eq. (18):

$$\begin{cases} f_1 = \frac{1}{2}c_1 + \frac{1}{2}c_1 + \frac{1}{2}d_2 + (-1)d_1 + \frac{1}{2}d_2, \\ f_2 = \frac{1}{8}c_1 + \frac{3}{4}c_1 + \frac{1}{8}c_2 + \frac{1}{8}d_2 + \frac{3}{8}d_1 + \frac{3}{8}d_2 + \frac{1}{8}d_3. \end{cases} \tag{21}$$

This rewriting required two implicit sample split operations on the right-hand side of each equation in (21).Finally, following step 3 of our *general construction* to reconstruct F_r, we form the following system of 3 linear equations in 3 unknowns (f_6,f_7, and f_8 in F_r):

$$\begin{cases} c_3 = \frac{1}{8}f_3 - \frac{1}{2}f_4 + \frac{3}{8}f_5 + f_6 + \frac{3}{8}f_7 - \frac{1}{2}f_8 + \frac{1}{8}f_7, \\ c_4 = \frac{1}{8}f_5 - \frac{1}{2}f_6 + \frac{3}{8}f_7 + f_8 + \frac{3}{8}f_7 - \frac{1}{2}f_6 + \frac{1}{8}f_5, \\ d_4 = -\frac{1}{8}f_5 + \frac{1}{2}f_6 - \frac{3}{4}f_7 + \frac{1}{2}f_8 - \frac{1}{8}f_7. \end{cases} \tag{22}$$

The equations in (22) were obtained from Fig. 10, which shows how c_3, c_4, and d_4 were evaluated during decomposition. Observe that in (22), we can replace f_3,f_4, and f_5 with the corresponding linear combinations of coarse and detail samples from Fig. 11. Then solving the 3×3 system formed by the equations in (22) gives

$$\begin{cases} f_6 = \frac{1}{8}c_2 + \frac{3}{4}c_3 + \frac{1}{8}c_4 + \frac{1}{8}d_2 + \frac{3}{8}d_3 + \frac{1}{2}d_4, \\ f_7 = \frac{1}{2}c_3 + \frac{1}{2}c_4 + \frac{1}{2}d_3 - \frac{1}{2}d_4, \\ f_8 = \frac{1}{4}c_3 + \frac{3}{4}c_4 + \frac{1}{4}d_3 + \frac{3}{4}d_4. \end{cases} \tag{23}$$

Now, the equations in (23) can be rewritten as follows such that the coefficients of the coarse and detail samples are all regular filters from Eq. (18):

$$\begin{cases} f_6 = \frac{1}{8}c_2 + \frac{3}{4}c_3 + \frac{1}{8}c_4 + \frac{1}{8}d_2 + \frac{3}{8}d_3 + \frac{3}{8}d_4 + \frac{1}{8}d_4, \\ f_7 = \frac{1}{2}c_3 + \frac{1}{2}c_4 + \frac{1}{2}d_3 + (-1)d_4 + \frac{1}{2}d_4, \\ f_8 = \frac{1}{8}c_3 + \frac{3}{4}c_4 + \frac{1}{8}c_3 + \frac{1}{8}d_3 + \frac{3}{8}d_4 + \frac{3}{8}d_4 + \frac{1}{8}d_3. \end{cases} \tag{24}$$

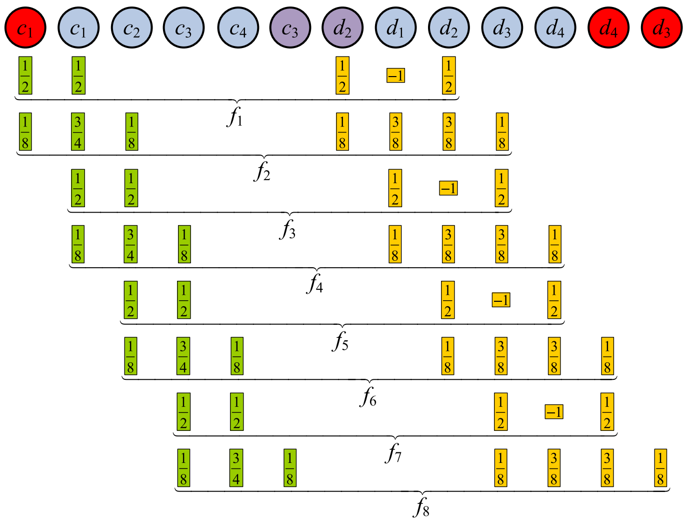

Fig. 12. Perfect reconstruction of 8 fine samples using the decomposition filter vectors **a** and **b** from Eq. (18).

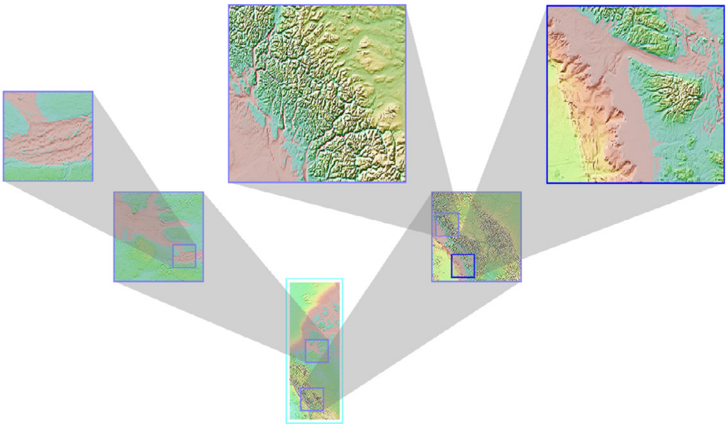

(a) Topographic and bathymetric shading of northwestern North America: $(4672\times12800, C_6, F^4, F^5, F^5, F^2, F^2)$.

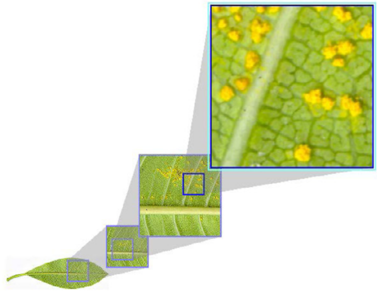

(c) Frangipani rust: $(10496\times3328, C_6, F^6, F^3, F^1)$.

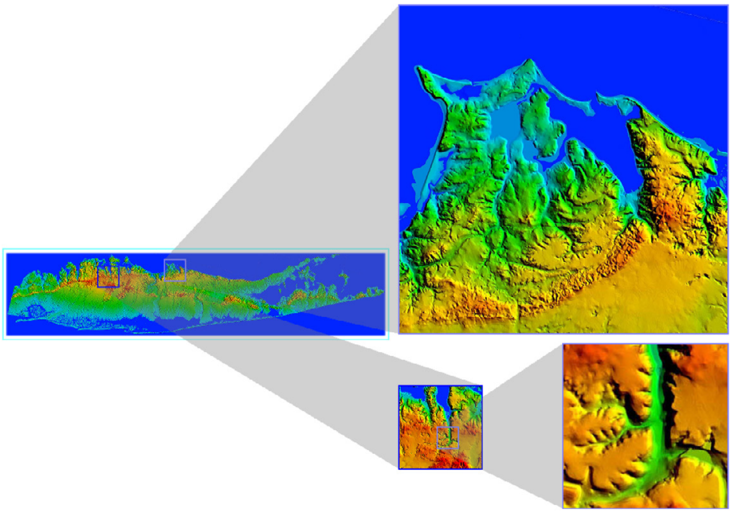

(b) Topographic shading of Long Island: $(18944\times4224, C_5, F^4, F^2, F^3)$.

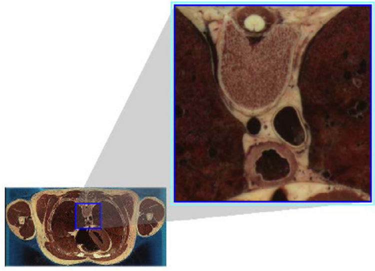

(d) Male abdomen: $(1728\times832, C_3, F^3)$.

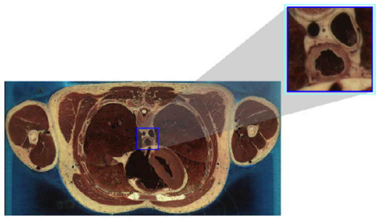

(e) Male abdomen: $(1728\times832, C_2, F^2)$.

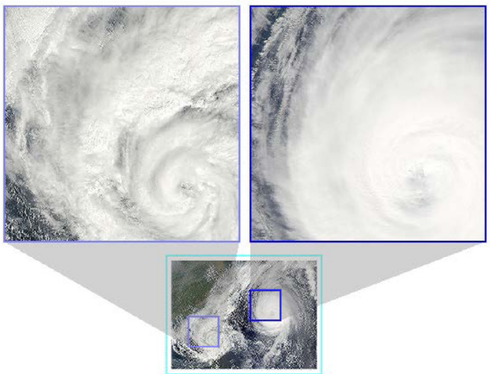

(f) Comparison of Parma (on the left) and Melor (on the right): $(10240\times7680, C_6, F^3, F^3)$.

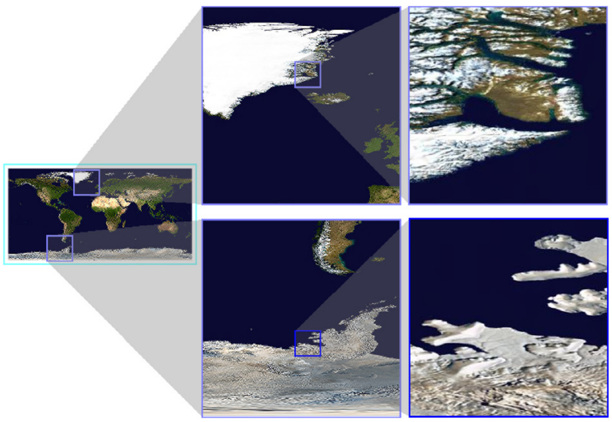

(g) Comparison of ice near the coasts of Greenland and Alexander Island: $(15360\times7680, C_6, F^3, F^3, F^3, F^3)$.

Fig. 13. Focus+context visualization of 2D images at various resolutions.

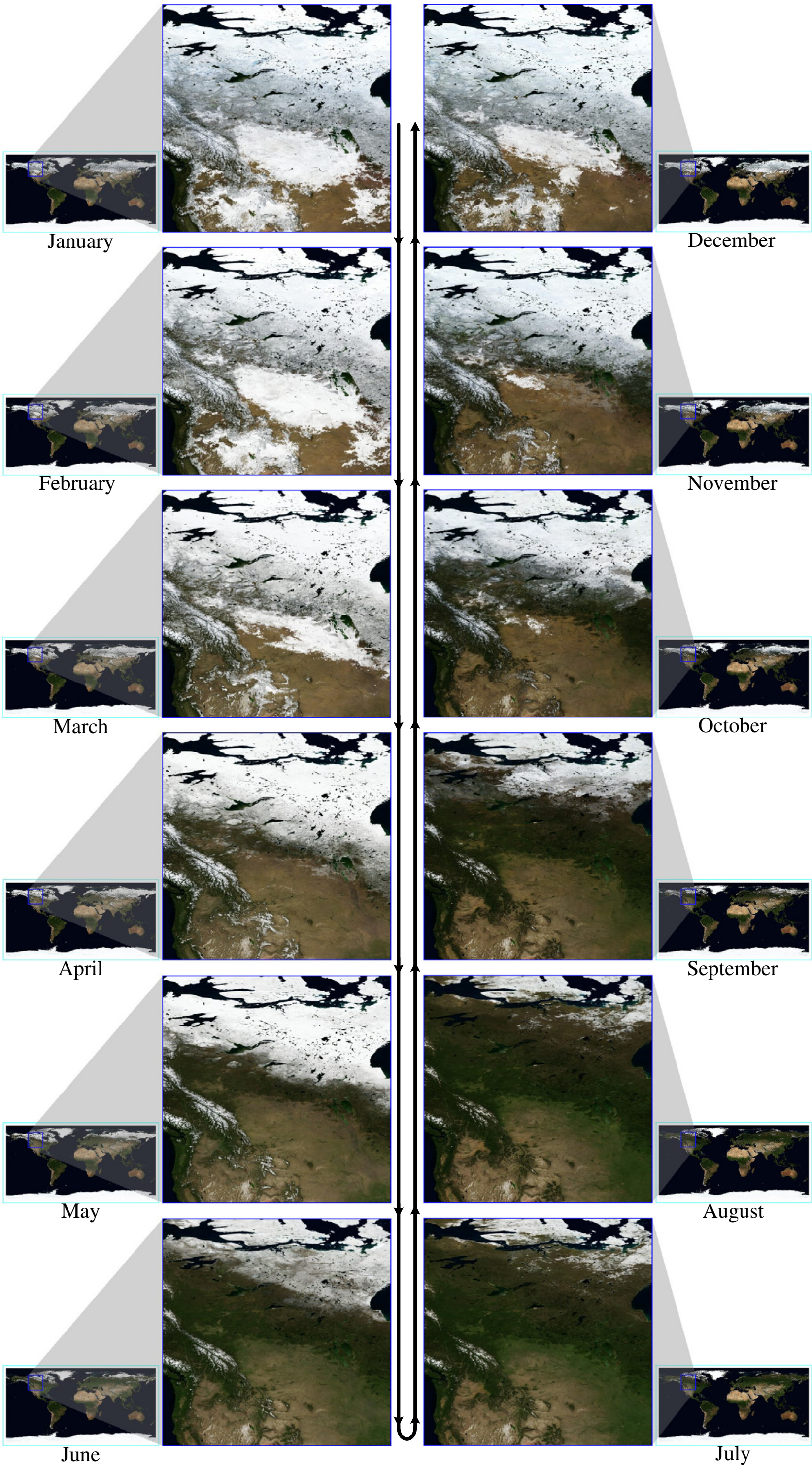

Fig. 14. Focus+context visualization of time-lapse imagery – monthly global images: $(5440 \times 2752 \times 12, C_4, F^4)$.

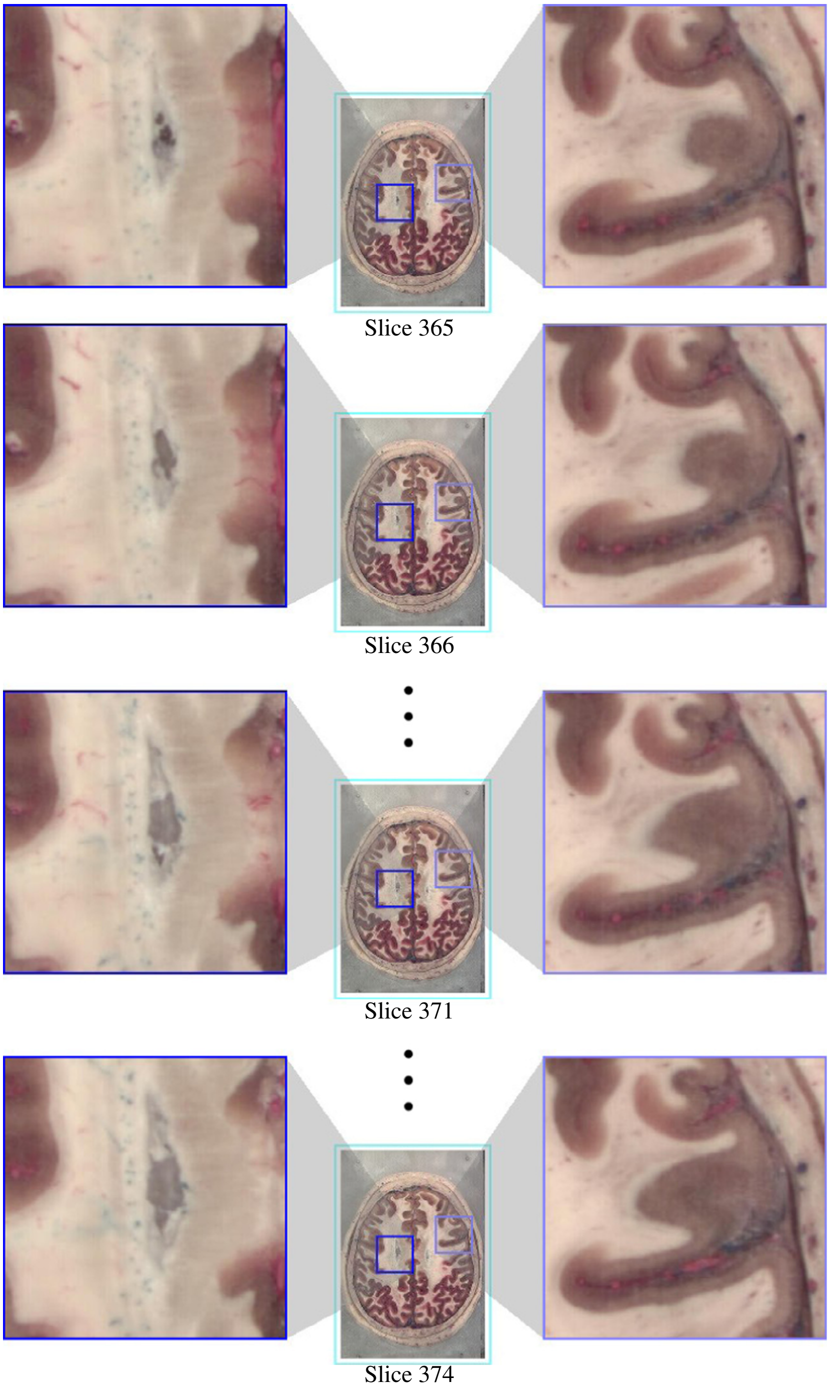

Fig. 15. Focus+context visualization of a 3D image – female head ($1056 \times 1528 \times 150, C_3, F^3, F^3$).

As we mentioned in the *general construction* given in Section 5.2, note that the equations in (21) and (24) yield a specific type of symmetric extension for each boundary of C and D as shown in Fig. 12. Therefore, based on (21) and (24), for a given column vector of $2n$ fine samples ($n \in \mathbb{Z}^+$), we get

$$\begin{cases} f_1 &= \frac{1}{2}c_1 + \frac{1}{2}c_1 + \frac{1}{2}d_2 + (-1)d_1 + \frac{1}{2}d_2, \\ f_2 &= \frac{1}{8}c_1 + \frac{3}{4}c_1 + \frac{1}{8}c_2 + \frac{1}{8}d_2 + \frac{3}{8}d_1 + \frac{3}{8}d_2 + \frac{1}{8}d_3, \\ f_{2n-2} &= \frac{1}{8}c_{n-2} + \frac{3}{4}c_{n-1} + \frac{1}{8}c_n + \frac{1}{8}d_{n-2} + \frac{3}{8}d_{n-1} + \frac{3}{8}d_n + \frac{1}{8}d_n, \\ f_{2n-1} &= \frac{1}{2}c_{n-1} + \frac{1}{2}c_n + \frac{1}{2}d_{n-1} + (-1)d_n + \frac{1}{2}d_n, \\ f_{2n} &= \frac{1}{8}c_{n-1} + \frac{3}{4}c_n + \frac{1}{8}c_{n-1} + \frac{1}{8}d_{n-1} + \frac{3}{8}d_n + \frac{3}{8}d_n + \frac{1}{8}d_{n-1}. \end{cases}$$

So a balanced multiresolution scheme based on the *inverse powers of two* filters of cubic B-spline given in Eq. (18) can make use of the matrix equation

$$\begin{bmatrix} f_1 \\ f_2 \\ \vdots \\ f_{2n} \end{bmatrix} = \begin{bmatrix} \frac{1}{2} & \frac{1}{2} & 0 & \cdots & 0 & 0 & 0 & 0 & 0 \\ \frac{1}{8} & \frac{3}{4} & \frac{1}{8} & \cdots & 0 & 0 & 0 & 0 & 0 \\ \vdots & \vdots & \vdots & \ddots & \vdots & \vdots & \vdots & \vdots & \vdots \\ 0 & 0 & 0 & \cdots & 0 & \frac{1}{8} & \frac{3}{4} & \frac{1}{8} & 0 \\ 0 & 0 & 0 & \cdots & 0 & 0 & \frac{1}{2} & \frac{1}{2} & 0 \\ 0 & 0 & 0 & \cdots & 0 & 0 & \frac{1}{8} & \frac{3}{4} & \frac{1}{8} \end{bmatrix} \begin{bmatrix} c_1 \\ c_1 \\ c_2 \\ \vdots \\ c_{n-1} \\ c_n \\ c_{n-1} \end{bmatrix} + \begin{bmatrix} \frac{1}{2} & -1 & \frac{1}{2} & 0 & \cdots & 0 & 0 & 0 & 0 & 0 \\ \frac{1}{8} & \frac{3}{8} & \frac{3}{8} & \frac{1}{8} & \cdots & 0 & 0 & 0 & 0 & 0 \\ \vdots & \vdots & \vdots & \vdots & \ddots & \vdots & \vdots & \vdots & \vdots & \vdots \\ 0 & 0 & 0 & 0 & \cdots & \frac{1}{8} & \frac{3}{8} & \frac{3}{8} & \frac{1}{8} & 0 \\ 0 & 0 & 0 & 0 & \cdots & 0 & \frac{1}{2} & -1 & \frac{1}{2} & 0 \\ 0 & 0 & 0 & 0 & \cdots & 0 & \frac{1}{8} & \frac{3}{8} & \frac{3}{8} & \frac{1}{8} \end{bmatrix} \begin{bmatrix} d_2 \\ d_1 \\ d_2 \\ \vdots \\ d_{n-1} \\ d_n \\ d_n \\ d_{n-1} \end{bmatrix} \tag{25}$$

for the reconstruction process, analogous to Eq. (3).

6. Application in focus+context visualization

Multiscale 2D and 3D image visualization applications often exploit query window-based focus+context visualization for image exploration and navigation purposes. A low-resolution approximation is rendered to provide the context and a selected portion of that low-resolution approximation defining the focus, also known as the ROI, is rendered as a close-up in high-resolution. While such visualization is supported by an underlying wavelet transform, it is necessary to reconstruct the high-resolution approximation of the ROI on demand from the low-resolution approximation and corresponding details. Here the use of a *balanced wavelet transform* constructed by our proposed method makes locating the details straightforward. For instance, observe the reconstruction of interior samples in Figs. 6 and 11. If the first coarse sample for the reconstruction of a fine sample is c_i, then first detail sample to use in the reconstruction of that fine sample is d_i. This may not have been the case if we had an unequal number of coarse and detail samples from decomposition. Also, the only additional step required to reconstruct the fine samples near the boundaries is the use of specific symmetric/antisymmetric extensions, because our method completely eliminates the need for extraordinary boundary filters.

6.1. Overview of visualization tool

We have implemented a visualization tool prototype named *Focus+Context Studio* to test our presented balanced multiresolution framework for images. It robustly allows real-time multilevel focus+context visualization of large-scale 2D and 3D images, supported by multiple movable query windows defining ROIs at different resolutions. It currently uses the balanced multiresolution scheme we devised using the *short* filters of quadratic B-spline in Eq. (4), as described in the examples shown in subSections 5.1 and 5.2. Therefore, it uses half-sample symmetric extensions for the sequences of fine samples during decomposition in the fashion shown in Fig. 5. On the other hand, for a perfect reconstruction, it uses half-sample symmetric extensions for the sequences of coarse samples and half-sample antisymmetric extensions for the sequences of detail samples in the manner shown in Fig. 7. The used balanced multiresolution scheme in its general form can be found in the second row of Table A.2. At the moment, all the query windows are 32×32 samples in dimension.

To facilitate focus+context visualization and exploration of a 3D image, our prototype currently allows the query windows identifying the ROIs to move back and forth through sequential slices interactively by the use of mouse scroll wheel and alternatively, the up and down arrow keys on the keyboard. When the query windows move from one slice to another, the low-resolution approximation of the context and the high-resolution approximations of the ROIs are updated on the fly in real-time. For 3D images, currently it only performs widthwise and heightwise decompositions, which keeps the number of 2D slices intact for depthwise volume exploration.

6.2. Experimental results

Here we present the experimental results produced by our *Focus+Context Studio* prototype. The n-tuples $(n \geqslant 3)$ used in the captions of Figs. 13–15 are defined as follows: (image dimensions, $C_d, F^{r_1}, F^{r_2}, \ldots, F^{r_m}$), where d is the number of levels of (widthwise and heightwise) decomposition for the context and $r_i (1 \leqslant i \leqslant m)$ is the number of levels of reconstruction for deriving the high-resolution approximation of the ith ROI. F^{r_i} appears in the n-tuple in a position determined by the left-to-right and top-to-bottom ordering of placement for the high-resolutions approximations of the ROIs.

Fig. 13 shows various scenarios for focus+context visualization of 2D images using our prototype. Figs. 13(a) and (b) show multilevel focus+context visualization of large-scale 2D images showing the topographic and bathymetric shading of northwestern North America (data source: D. Sandwell et al., University of California San Diago, USA) and the topographic shading of Long Island (data source: G. Hanson, Stony Brook University, USA), respectively. Similar multilevel focus+context visualization is shown for a diseased leaf (data source: S. Fraser-Smith, Wikipedia) in Fig. 13(c). Such multilevel focus+context visualization is motivated by the need for more manageable utilization of screen space and visualization of the context at a higher resolution while maintaining interactive frame rates.

Next, for a 2D image, Figs. 13(d) and (e) show different levels of decomposition for the context and different levels of reconstruction for the high-resolution approximation of the ROI using our developed tool. The 2D image used in this example is an abdomen slice from a male (data source: Male Abdomen, The Visible Human Project, U.S. National

Library of Medicine). One advantage of allowing multiple query windows corresponding to multiple ROIs is the ability to draw comparisons between similar ROIs when required. Fig. 13(f) shows such a comparison scenario between the tropical storm Parma on the left and typhoon Melor on the right (data source: MODIS Rapid Response Team, NASA). Another such scenario comparing the ice near the coasts of Greenland and Alexander Island (data source: Visible Earth, NASA) is shown in Fig. 13(g).

Our developed prototype is also suitable for the visualization and exploration of time-lapse imagery. For instance, Fig. 14 shows 12 unique frames from the interactive transition through the 12 slices of monthly global images (data source: R. Stöckli, Monthly Global Images, NASA). The order of frames is shown by directions marked on the curved-arrow in the middle. The ROI covers most of northwestern North America and shows the transition from one winter to the following winter.

which 150 sequential slices were loaded into our prototype for this example.

7. Discussion and future work

Not using the type of symmetric extension suggested by our *general construction* in Section 5.1 to obtain the extra fine samples required for a balanced decomposition may lead to the use of extraordinary boundary filters. For the sake of comparison, we used half-sample symmetric extension in place of the suggested whole-sample symmetric extension to obtain the five extra fine samples required for a balanced decomposition using the decomposition filter vectors in Eq. (A.3), which contains the *wide* and *optimal* filters of cubic B-spline. This led to the following matrix equation for a perfect reconstruction, both **P** and **Q** matrices containing unwanted extraordinary boundary filters:

$$
\begin{bmatrix} f_1 \\ f_2 \\ \vdots \\ f_{2n} \end{bmatrix} =
\left[\begin{array}{cccccccc}
\frac{11}{10} & -\frac{1}{10} & 0 & \cdots & 0 & 0 & 0 & 0 \\
\frac{9}{10} & \frac{1}{10} & 0 & \cdots & 0 & 0 & 0 & 0 \\
\hline
\frac{1}{2} & \frac{1}{2} & 0 & \cdots & 0 & 0 & 0 & 0 \\
\frac{1}{8} & \frac{3}{4} & \frac{1}{8} & \cdots & 0 & 0 & 0 & 0 \\
\vdots & \vdots & \vdots & \ddots & \vdots & \vdots & \vdots & \vdots \\
0 & 0 & 0 & \cdots & \frac{1}{8} & \frac{3}{4} & \frac{1}{8} & 0 \\
0 & 0 & 0 & \cdots & 0 & \frac{1}{2} & \frac{1}{2} & 0 \\
\hline
0 & 0 & 0 & \cdots & 0 & \frac{1199}{9730} & \frac{1472}{1946} & \frac{84}{695} \\
0 & 0 & 0 & \cdots & 0 & -\frac{69}{9730} & \frac{1019}{1946} & \frac{336}{695} \\
0 & 0 & 0 & \cdots & 0 & -\frac{23}{1946} & \frac{401}{1946} & \frac{112}{139}
\end{array}\right]
\begin{bmatrix} c_1 \\ c_2 \\ \vdots \\ c_n \end{bmatrix}
+
\left[\begin{array}{ccccccccc}
\frac{263}{52} & -\frac{82}{65} & \frac{23}{260} & 0 & \cdots & 0 & 0 & 0 & 0 \\
\frac{37}{52} & -\frac{33}{65} & -\frac{23}{260} & 0 & \cdots & 0 & 0 & 0 & 0 \\
\hline
-\frac{23}{52} & 1 & -\frac{23}{52} & 0 & \cdots & 0 & 0 & 0 & 0 \\
-\frac{23}{208} & -\frac{63}{208} & -\frac{63}{208} & -\frac{23}{208} & \cdots & 0 & 0 & 0 & 0 \\
\vdots & \vdots & \vdots & \vdots & \ddots & \vdots & \vdots & \vdots & \vdots \\
0 & 0 & 0 & 0 & \cdots & -\frac{23}{208} & -\frac{63}{208} & -\frac{63}{208} & -\frac{23}{208} \\
0 & 0 & 0 & 0 & \cdots & 0 & -\frac{23}{52} & 1 & -\frac{23}{52} \\
\hline
0 & 0 & 0 & 0 & \cdots & 0 & -\frac{27577}{252980} & -\frac{566}{1807} & -\frac{4841}{19460} \\
0 & 0 & 0 & 0 & \cdots & 0 & \frac{1587}{252980} & -\frac{874}{1807} & \frac{307743}{252980} \\
0 & 0 & 0 & 0 & \cdots & 0 & \frac{529}{50596} & -\frac{391}{1807} & \frac{5281}{50596}
\end{array}\right]
\begin{bmatrix} d_1 \\ d_2 \\ \vdots \\ d_n \end{bmatrix}
$$

in place of Eq. (A.4). Note that such extraordinary boundary filters in **P** and **Q** matrices do not allow the anticipated sample split operations that yield suitable symmetric/antisymmetric extensions to use for C and D for a perfect reconstruction only by the use of regular filters.

Our method can be used to devise a balanced multiresolution scheme for any set of given regular multiresolution

Fig. 15 shows an example of visualization and exploration of a 3D image in our prototype. For the purpose of demonstration, the transition through 10 of the 150 slices that the query windows were constrained to move back and forth through are shown in Fig. 15 (data source: Female head, The Visible Human Project, U.S. National Library of Medicine). This head dataset contains a total of 1477 2D slices, each of dimensions 1056×1528, among filter vectors. However, if the scheme would only make use of regular reconstruction filters is determined by the properties of the given multiresolution filter vectors. If the given filter vectors are symmetric/antisymmetric, then our method can devise a balanced multiresolution scheme that only uses regular filters. Otherwise, some extraordinary boundary reconstruction filters are introduced (see B, for instance).

The balanced multiresolution schemes devised by our approach can also be applied to open curves and tensor product meshes (surfaces and volumes) in applications where boundary interpolation is not important but a balanced decomposition is preferred, for reasons such as partitioning the curve or the mesh into *even* and *odd* vertices. Such a partitioning allows the storage of coarse vertices and details in even and odd vertices, respectively, as proposed in [22]. However, some of the devised balanced multiresolution schemes may support boundary interpolation only in the context of subdivision i.e. when we only consider the result of $\mathbf{P}C'$ in order to increase the resolution of C. For example, the filters of second order B-spline in Eq. (A.1) and the *short* filters of third order B-spline in Eq. (4) lead to such boundary interpolating subdivisions.

There is a number of directions for future research. In this article, we covered the commonly used types of symmetric and antisymmetric extensions. It would be useful to investigate and develop extension types that can be utilized to devise balanced multiresolution schemes for near symmetric and asymmetric filter vectors in order to ensure a perfect reconstruction solely by the use of regular filters. To start with, the devised balanced multiresolution scheme given in B for Daubechies' asymmetric D4 filters may provide some insights.

In addition, further investigations are needed for an in-depth understanding of the relations between the symmetry/antisymmetry exhibited by the filter vectors, parity of their widths, and the determined types of symmetric/antisymmetric extensions required for a perfect reconstruction using only regular filters. For instance, compare the multiresolution filter vectors containing the *inverse powers of two* filters of fourth order B-spline in Eq. (18) and the *wide* and *optimal* filters of fourth order B-spline in Eq. (A.3). In these two sets, the corresponding filter vectors have the same widths and they are all symmetric. Now, observe that the two balanced multiresolution schemes we devised using these two sets of filter vectors suggest exactly the same type of symmetric extensions for the column vectors of fine, coarse, and detail samples. Therefore, the determined types of symmetric/antisymmetric extensions are not dependant on actual filter values. Several other such scenarios are shown in Table A.2.

From application's standpoint, our current implementation supporting focus+context visualization of 3D images (see Fig. 15, for example) can be extended by additionally performing depthwise balanced decompositions and allowing 3D ROIs that are not necessarily axis-aligned. These will facilitate a more flexible visualization framework for large-scale 3D images.

8. Conclusion

In this article, we presented a novel method for devising a *balanced multiresolution* scheme, primarily applicable to images, using a given set of symmetric/antisymmetric filter vectors containing regular multiresolution filters. A balanced multiresolution scheme resulting from our method allows balanced decomposition and subsequent perfect reconstruction of images without using any extraordinary boundary filters. This is achieved by the use of an appropriate combination of symmetric and antisymmetric extensions at the image and detail boundaries, correlating to implicit sample split operations. Balanced wavelet transform of an image constructed through balanced decompositions provides straightforward and efficient access to details corresponding to a ROI on demand.

In order to support smooth multiresolution representations of images beyond Haar wavelets and the associated scaling functions, and still exploit the advantages of a balanced decomposition, we used our method to devise balanced multiresolution schemes for some commonly used sets of local multiresolution filters obtained from higher order scaling functions and their wavelets. Any such balanced multiresolution scheme can be used to generate a *balanced wavelet transform* representation of a multidimensional image in a preprocessing phase, which can then be utilized to support its focus+context visualization in an efficient manner.

We also presented a set of experimental results produced using our developed *Focus+Context Studio* prototype that allows interactive multilevel focus+context visualization of large-scale 2D and 3D images. It exploits the balanced multiresolution scheme we devised from the *short* filters of quadratic B-spline in Eq. (4). We envision the integration of the key functionalities of our prototype in visualization systems and application programming interfaces (APIs) to enable users to visualize and explore the contents of complex imagery such as large-scale satellite images, clinical data, seismic data, etc.

Acknowledgements

We would to thank Javad Sadeghi for providing the multiresolution filter vectors containing the local filters of second order B-spline in Eq. (A.1) and Jennifer E. Fairman for providing the traditional medical illustration shown in Fig. 4(a). We would also like to thank Troy Alderson for his helpful editorial comments.

Appendix A. Further examples with symmetric/antisymmetric filter vectors

Our first example here involves the multiresolution filter vectors containing the local regular filters of second order B-spline,

$$\begin{cases} \mathbf{a} &= \left[-\frac{1}{6} \quad \frac{1}{3} \quad \frac{2}{3} \quad \frac{1}{3} \quad -\frac{1}{6}\right], \\ \mathbf{b} &= \left[-\frac{1}{2} \quad 1 \quad -\frac{1}{2}\right], \\ \mathbf{p} &= \left[\frac{1}{2} \quad 1 \quad \frac{1}{2}\right], \\ \mathbf{q} &= \left[-\frac{1}{6} \quad -\frac{1}{3} \quad \frac{2}{3} \quad -\frac{1}{3} \quad -\frac{1}{6}\right], \end{cases} \tag{A.1}$$

derived by Sadeghi [25] by reversing Faber subdivision [9] based on the construction procedure presented by Samavati and Bartels in [26,3]. For the filter vectors in Eq. (A.1), the matrix equations for a balanced multiresolution scheme we devised using our method for $n \in \mathbb{Z}^+$ are

$$\begin{bmatrix} c_1 \\ c_2 \\ \vdots \\ c_n \end{bmatrix} = \begin{bmatrix} -\frac{1}{6} & \frac{1}{3} & \frac{2}{3} & \frac{1}{3} & -\frac{1}{6} & 0 & 0 & 0 & \cdots \\ 0 & 0 & -\frac{1}{6} & \frac{1}{3} & \frac{2}{3} & \frac{1}{3} & -\frac{1}{6} & 0 & \cdots \\ \vdots & \vdots & \vdots & \vdots & \vdots & \vdots & \vdots & \vdots & \ddots \end{bmatrix} \begin{bmatrix} f_2 \\ f_1 \\ f_2 \\ \vdots \\ f_{2n-1} \\ f_{2n} \\ f_{2n-1} \\ f_{2n-2} \end{bmatrix},$$

$$\begin{bmatrix} d_1 \\ d_2 \\ \vdots \\ d_n \end{bmatrix} = \begin{bmatrix} -\frac{1}{2} & 1 & -\frac{1}{2} & 0 & 0 & 0 & \cdots \\ 0 & 0 & -\frac{1}{2} & 1 & -\frac{1}{2} & 0 & \cdots \\ \vdots & \vdots & \vdots & \vdots & \vdots & \vdots & \ddots \end{bmatrix} \begin{bmatrix} f_2 \\ f_1 \\ f_2 \\ \vdots \\ f_{2n} \end{bmatrix},$$

and

$$\begin{bmatrix} f_1 \\ f_2 \\ \vdots \\ f_{2n} \end{bmatrix} = \begin{bmatrix} \frac{1}{2} & \frac{1}{2} & 0 & \cdots & 0 & 0 \\ 0 & 1 & 0 & \cdots & 0 & 0 \\ 0 & \frac{1}{2} & \frac{1}{2} & \cdots & 0 & 0 \\ \vdots & \vdots & \vdots & \ddots & \vdots & \vdots \\ 0 & 0 & 0 & \cdots & \frac{1}{2} & \frac{1}{2} \\ 0 & 0 & 0 & \vdots & 0 & 1 \end{bmatrix} \begin{bmatrix} c_1 \\ c_1 \\ c_2 \\ \vdots \\ c_n \end{bmatrix} + \begin{bmatrix} -\frac{1}{6} & \frac{2}{3} & -\frac{1}{6} & 0 & \cdots & 0 & 0 & 0 \\ 0 & -\frac{1}{3} & -\frac{1}{3} & 0 & \cdots & 0 & 0 & 0 \\ 0 & -\frac{1}{6} & \frac{2}{3} & -\frac{1}{6} & \cdots & 0 & 0 & 0 \\ \vdots & \vdots & \vdots & \vdots & \ddots & \vdots & \vdots & \vdots \\ 0 & 0 & 0 & 0 & \cdots & -\frac{1}{6} & \frac{2}{3} & -\frac{1}{6} \\ 0 & 0 & 0 & 0 & \cdots & 0 & -\frac{1}{3} & -\frac{1}{3} \end{bmatrix} \begin{bmatrix} d_2 \\ d_1 \\ d_2 \\ \vdots \\ d_n \\ d_n \end{bmatrix},$$

analogous to Eqs. (1)–(3), respectively.

The next example involves the following multiresolution filter vectors containing the local regular filters of cubic (fourth order) B-spline from [28]:

$$\begin{cases} \mathbf{a} &= \left[-\frac{1}{2} \;\; 2 \;\; -\frac{1}{2}\right], \\ \mathbf{b} &= \left[\frac{1}{4} \;\; -1 \;\; \frac{3}{2} \;\; -1 \;\; \frac{1}{4}\right], \\ \mathbf{p} &= \left[\frac{1}{8} \;\; \frac{1}{2} \;\; \frac{3}{4} \;\; \frac{1}{2} \;\; \frac{1}{8}\right], \\ \mathbf{q} &= \left[\frac{1}{4} \;\; 1 \;\; \frac{1}{4}\right]. \end{cases} \tag{A.2}$$

The filter vectors in Eq. (A.2) are called the *short* filters of cubic B-spline. For these filter vectors, the matrix equations for a balanced multiresolution scheme we devised using our method for $n \in \mathbb{Z}^+$ are

$$\begin{bmatrix} c_1 \\ c_2 \\ \vdots \\ c_n \end{bmatrix} = \begin{bmatrix} -\frac{1}{2} & 2 & -\frac{1}{2} & 0 & 0 & 0 & \cdots \\ 0 & 0 & -\frac{1}{2} & 2 & -\frac{1}{2} & 0 & \cdots \\ \vdots & \vdots & \vdots & \vdots & \vdots & \vdots & \ddots \end{bmatrix} \begin{bmatrix} f_2 \\ f_1 \\ f_2 \\ \vdots \\ f_{2n} \end{bmatrix},$$

$$\begin{bmatrix} d_1 \\ d_2 \\ \vdots \\ d_n \end{bmatrix} = \begin{bmatrix} \frac{1}{4} & -1 & \frac{3}{2} & -1 & \frac{1}{4} & 0 & 0 & 0 & \cdots \\ 0 & 0 & \frac{1}{4} & -1 & \frac{3}{2} & -1 & \frac{1}{4} & 0 & \cdots \\ \vdots & \vdots & \vdots & \vdots & \vdots & \vdots & \vdots & \vdots & \ddots \end{bmatrix} \begin{bmatrix} f_2 \\ f_1 \\ f_2 \\ \vdots \\ f_{2n-1} \\ f_{2n} \\ f_{2n-1} \\ f_{2n-2} \end{bmatrix},$$

and

$$\begin{bmatrix} f_1 \\ f_2 \\ \vdots \\ f_{2n} \end{bmatrix} = \begin{bmatrix} \frac{1}{8} & \frac{3}{4} & \frac{1}{8} & 0 & \cdots & 0 & 0 & 0 \\ 0 & \frac{1}{2} & \frac{1}{2} & 0 & \cdots & 0 & 0 & 0 \\ 0 & \frac{1}{8} & \frac{3}{4} & \frac{1}{8} & \cdots & 0 & 0 & 0 \\ \vdots & \vdots & \vdots & \vdots & \ddots & \vdots & \vdots & \vdots \\ 0 & 0 & 0 & 0 & \cdots & \frac{1}{8} & \frac{3}{4} & \frac{1}{8} \\ 0 & 0 & 0 & 0 & \cdots & 0 & \frac{1}{2} & \frac{1}{2} \end{bmatrix} \begin{bmatrix} c_2 \\ c_1 \\ c_2 \\ \vdots \\ c_n \\ c_n \end{bmatrix} + \begin{bmatrix} \frac{1}{4} & \frac{1}{4} & 0 & \cdots & 0 & 0 \\ 0 & 1 & 0 & \cdots & 0 & 0 \\ 0 & \frac{1}{4} & \frac{1}{4} & \cdots & 0 & 0 \\ \vdots & \vdots & \vdots & \ddots & \vdots & \vdots \\ 0 & 0 & 0 & \cdots & \frac{1}{4} & \frac{1}{4} \\ 0 & 0 & 0 & \vdots & 0 & 1 \end{bmatrix} \begin{bmatrix} d_1 \\ d_1 \\ d_2 \\ \vdots \\ d_n \end{bmatrix},$$

analogous to Eqs. (1)–(3), respectively.

Our last example uses the following multiresolution filter vectors containing the local regular filters of cubic B-spline from [28]:

$$\begin{cases} \mathbf{a} &= \left[\frac{23}{196} \;\; -\frac{23}{49} \;\; \frac{9}{28} \;\; \frac{52}{49} \;\; \frac{9}{28} \;\; -\frac{23}{49} \;\; \frac{23}{196}\right], \\ \mathbf{b} &= \left[\frac{13}{98} \;\; -\frac{26}{49} \;\; \frac{39}{49} \;\; -\frac{26}{49} \;\; \frac{13}{98}\right], \\ \mathbf{p} &= \left[\frac{1}{8} \;\; \frac{1}{2} \;\; \frac{3}{4} \;\; \frac{1}{2} \;\; \frac{1}{8}\right], \\ \mathbf{q} &= \left[-\frac{23}{208} \;\; -\frac{23}{52} \;\; -\frac{63}{208} \;\; 1 \;\; -\frac{63}{208} \;\; -\frac{23}{52} \;\; -\frac{23}{208}\right]. \end{cases} \tag{A.3}$$

The filter vectors in Eq. (A.3) are known as the *wide* and *optimal* filters of cubic B-spline. For these filter vectors, the matrix equations for a balanced multiresolution scheme we devised using our method for $n \in \mathbb{Z}^+$ are

$$\begin{bmatrix} c_1 \\ c_2 \\ \vdots \\ c_n \end{bmatrix} = \begin{bmatrix} \frac{23}{196} & -\frac{23}{49} & \frac{9}{28} & \frac{52}{49} & \frac{9}{28} & -\frac{23}{49} & \frac{23}{196} & 0 & 0 & 0 & \cdots \\ 0 & 0 & \frac{23}{196} & -\frac{23}{49} & \frac{9}{28} & \frac{52}{49} & \frac{9}{28} & -\frac{23}{49} & \frac{23}{196} & 0 & \cdots \\ \vdots & \vdots & \vdots & \vdots & \vdots & \vdots & \vdots & \vdots & \vdots & \vdots & \ddots \end{bmatrix} \begin{bmatrix} f_3 \\ f_2 \\ f_1 \\ f_2 \\ \vdots \\ f_{2n-1} \\ f_{2n} \\ f_{2n-1} \\ f_{2n-2} \\ f_{2n-3} \end{bmatrix},$$

Table A.2
Balanced multiresolution schemes.

Filters	**a**	**b**	**p**	**q**	w_a, w_b	Decomposition: F', c_1, d_1	Reconstruction: $C', D', f_i \in \left[F_l^T F_r^T\right]^T$
Filters of second order B-spline (A.1) Biorthogonal 2.2 filters (**a**, **b**, **p**, and**q** in [20])	S	S	S	S	Odd	$F' = [f_2 f_1 \ldots f_{2n} f_{2n-1} f_{2n-2}]^T$, $\left\{\begin{array}{lcl} c_1 & = & a_{-2}f_2 + a_{-1}f_1 + a_0 f_2 \\ & & +a_1 f_3 + a_2 f_4, \\ d_1 & = & b_{-1}f_2 + b_0 f_1 + b_1 f_2. \end{array}\right.$	$C' = [c_1 c_1 \ldots c_n]^T, D' = [d_2 d_1 \ldots d_n d_n]^T$, $\left\{\begin{array}{lcl} f_1 & = & p_1 c_1 + p_{-1}c_1 + q_2 d_2 + q_0 d_1 + q_{-2}d_2, \\ f_{2n-1} & = & p_1 c_{n-1} + p_{-1}c_n + q_2 d_{n-1} + q_0 d_n + q_{-2}d_n, \\ f_{2n} & = & p_0 c_n + q_1 d_n + q_{-1}d_n. \end{array}\right.$
Short filters of quadratic B-spline (4) Biorthogonal 3.1 filters (**a**, **b**, **p**, and$\mathbf{q}^R$ in [20]) Reverse biorthogonal 3.1 filters (**a**, **b**, **p**, and$\mathbf{q}^R$ in [20])	S	A	S	A	Even	$F' = [f_1 f_1 \ldots f_{2n} f_{2n}]^T$, $\left\{\begin{array}{lcl} c_1 & = & a_{-2}f_1 + a_{-1}f_1 + a_1 f_2 + a_2 f_3, \\ d_1 & = & b_{-2}f_1 + b_{-1}f_1 + b_1 f_2 + b_2 f_3. \end{array}\right.$	$C' = [c_1 c_1 \ldots c_n c_n]^T, D' = [-d_1 d_1 \ldots d_n - d_n]^T$, $\left\{\begin{array}{lcl} f_1 & = & p_2 c_1 + p_{-1}c_1 + q_2(-d_1) + q_{-1}d_1, \\ f_{2n} & = & p_1 c_n + p_{-2}c_n + q_1 d_n + q_{-2}(-d_n). \end{array}\right.$
Wide filters of quadratic B-spline (**a**, **b**, **p**, and**q** in [28]) Biorthogonal 3.3 filters (**a**, **b**, **p**, and$\mathbf{q}^R$ in [20])	S	A	S	A	Even	$F' = [f_3 f_2 f_1 f_1 \ldots f_{2n} f_{2n} f_{2n-1} f_{2n-2}]^T$, $\left\{\begin{array}{lcl} c_1 & = & a_{-4}f_3 + a_{-3}f_2 + a_{-2}f_1 + a_{-1}f_1 \\ & & +a_1 f_2 + a_2 f_3 + a_3 f_4 + d_4 f_5, \\ d_1 & = & b_{-2}f_1 + b_{-1}f_1 + b_1 f_2 + b_2 f_3. \end{array}\right.$	$C' = [c_1 c_1 \ldots c_n c_n]^T, D' = [-d_2 - d_1 d_1 \ldots d_n - d_n - d_{n-1}]^T$, $\left\{\begin{array}{lcl} f_1 & = & p_2 c_1 + p_{-1}c_1 + q_4(-d_2) + q_2(-d_1) + q_{-1}d_1 + q_{-3}d_2, \\ f_2 & = & p_1 c_1 + p_{-2}c_2 + q_3(-d_1) + q_1 d_1 + q_{-2}d_2 + q_{-4}d_3, \\ f_3 & = & p_2 c_1 + p_{-1}c_2 + q_4(-d_1) + q_2 d_1 + q_{-1}d_2 + q_{-3}d_3, \\ f_{2n-2} & = & p_1 c_{n-1} + p_{-2}c_n + q_3 d_{n-2} + q_1 d_{n-1} + q_{-2}d_n + q_{-4}(-d_n), \\ f_{2n-1} & = & p_2 c_{n-1} + p_{-1}c_n + q_4 d_{n-2} + q_2 d_{n-1} + q_{-1}d_n + q_{-3}(-d_n), \\ f_{2n} & = & p_1 c_n + p_{-2}c_n + q_3 d_{n-1} + q_1 d_n + q_{-2} - d_n + q_{-4}(-d_{n-1}). \end{array}\right.$
Short filters of cubic B-spline (A.2) Reverse biorthogonal 2.2 filters (**a**, **b**, **p**, and**q** in [20])	S	S	S	S	Odd	$F' = [f_2 f_1 \ldots f_{2n} f_{2n-1} f_{2n-2}]^T$, $\left\{\begin{array}{lcl} c_1 & = & a_{-1}f_2 + a_0 f_1 + a_1 f_2, \\ d_1 & = & b_{-2}f_2 + b_{-1}f_1 + b_0 f_2 \\ & & +b_1 f_3 + b_2 f_4. \end{array}\right.$	$C' = [c_2 c_1 \ldots c_n c_n]^T, D' = [d_1 d_1 \ldots d_n]^T$, $\left\{\begin{array}{lcl} f_1 & = & p_2 c_2 + p_0 c_1 + p_{-2}c_2 + q_1 d_1 + q_{-1}d_1, \\ f_{2n-1} & = & p_2 c_{n-1} + p_0 c_n + p_{-2}c_n + q_1 d_{n-1} + q_{-1}d_n, \\ f_{2n} & = & p_1 c_n + p_{-1}c_n + q_0 d_n. \end{array}\right.$
Inverse powers of two filters of cubic B-spline (18) *Wide* and *optimal* filters of cubic B-spline (A.3)	S	S	S	S	Odd	$F' = [f_3 f_2 f_1 \ldots f_{2n} f_{2n-1} f_{2n-2} f_{2n-3}]^T$, $\left\{\begin{array}{lcl} c_1 & = & a_{-3}f_3 + a_{-2}f_2 + a_{-1}f_1 + a_0 f_2 \\ & & +a_1 f_3 + a_2 f_4 + a_3 f_5, \\ d_1 & = & b_{-2}f_3 + b_{-1}f_2 + b_0 f_1 \\ & & +b_1 f_2 + b_2 f_3. \end{array}\right.$	$C' = [c_1 c_1 \ldots c_n c_{n-1}]^T, D' = [d_2 d_1 \ldots d_n d_n d_{n-1}]^T$, $\left\{\begin{array}{lcl} f_1 & = & p_1 c_1 + p_{-1}c_1 + q_2 d_2 + q_0 d_1 + q_{-2}d_2, \\ f_2 & = & p_2 c_1 + p_0 c_1 + p_{-2}c_2 + q_3 d_2 + q_1 d_1 + q_{-1}d_2 + q_{-3}d_3, \\ f_{2n-2} & = & p_2 c_{n-2} + p_0 c_{n-1} + p_{-2}c_n + q_3 d_{n-2} + q_1 d_{n-1} + q_{-1}d_n + q_{-3}d_n, \\ f_{2n-1} & = & p_1 c_{n-1} + p_{-1}c_n + q_2 d_{n-1} + q_0 d_n + q_{-2}d_n, \\ f_{2n} & = & p_2 c_{n-1} + p_0 c_n + p_{-2}c_{n-1} + q_3 d_{n-1} + q_1 d_n + q_{-1}d_n + q_{-3}d_{n-1}. \end{array}\right.$

$$\begin{bmatrix} d_1 \\ d_2 \\ \vdots \\ d_n \end{bmatrix} = \begin{bmatrix} \frac{13}{98} & -\frac{26}{49} & \frac{39}{49} & -\frac{26}{49} & \frac{13}{98} & 0 & 0 & 0 & \cdots \\ 0 & 0 & \frac{13}{98} & -\frac{26}{49} & \frac{39}{49} & -\frac{26}{49} & \frac{13}{98} & 0 & \cdots \\ \vdots & \vdots & \vdots & \vdots & \vdots & \vdots & \vdots & \vdots & \ddots \end{bmatrix} \begin{bmatrix} f_3 \\ f_2 \\ f_1 \\ f_2 \\ \vdots \\ f_{2n-1} \\ f_{2n} \\ f_{2n-1} \end{bmatrix},$$

and

$$\begin{bmatrix} f_1 \\ f_2 \\ \vdots \\ f_{2n} \end{bmatrix} = \begin{bmatrix} \frac{1}{2} & \frac{1}{2} & 0 & \cdots & 0 & 0 & 0 & 0 & 0 \\ \frac{1}{8} & \frac{3}{4} & \frac{1}{8} & \cdots & 0 & 0 & 0 & 0 & 0 \\ \vdots & \vdots & \vdots & \ddots & \vdots & \vdots & \vdots & \vdots & \vdots \\ 0 & 0 & 0 & \cdots & 0 & \frac{1}{8} & \frac{3}{4} & \frac{1}{8} & 0 \\ 0 & 0 & 0 & \cdots & 0 & 0 & \frac{1}{2} & \frac{1}{2} & 0 \\ 0 & 0 & 0 & \cdots & 0 & 0 & \frac{1}{8} & \frac{3}{4} & \frac{1}{8} \end{bmatrix} \begin{bmatrix} c_1 \\ c_1 \\ c_2 \\ \vdots \\ c_{n-1} \\ c_n \\ c_{n-1} \end{bmatrix}$$
$$+ \begin{bmatrix} -\frac{23}{52} & 1 & -\frac{23}{52} & 0 & \cdots & 0 & 0 & 0 & 0 & 0 \\ -\frac{23}{208} & -\frac{63}{208} & -\frac{63}{208} & -\frac{23}{208} & \cdots & 0 & 0 & 0 & 0 & 0 \\ \vdots & \vdots & \vdots & \vdots & \ddots & \vdots & \vdots & \vdots & \vdots & \vdots \\ 0 & 0 & 0 & 0 & \cdots & -\frac{23}{208} & -\frac{63}{208} & -\frac{63}{208} & -\frac{23}{208} & 0 \\ 0 & 0 & 0 & 0 & \cdots & 0 & -\frac{23}{52} & 1 & -\frac{23}{52} & 0 \\ 0 & 0 & 0 & 0 & \cdots & 0 & -\frac{23}{208} & -\frac{63}{208} & -\frac{63}{208} & -\frac{23}{208} \end{bmatrix} \begin{bmatrix} d_2 \\ d_1 \\ d_2 \\ \vdots \\ d_{n-1} \\ d_n \\ d_n \\ d_{n-1} \end{bmatrix}, \tag{A.4}$$

analogous to Eqs. (1)–(3), respectively.

In Table A.2, we summarize all the balanced multiresolution schemes presented in this article so far, in addition to six other sets of symmetric/antisymmetric regular multiresolution filters. The biorthogonal and reverse biorthogonal filters [5,8] we referred to in the table are available in MATLAB [20].

In the first column of In Table A.2, $\mathbf{q}^R$ denotes the reversed filter vector $\mathbf{q}$. The second through fifth columns specify the symmetric (S)/antisymmetric (A) structure of the $\mathbf{a}, \mathbf{b}, \mathbf{p}$, and $\mathbf{q}$ filter vectors, respectively, for each set of filters in the table. The next column mentions the parity of w_a and w_b, based on which we decide on the type of symmetric extension to use for F.

For $n \in \mathbb{Z}^+$, the second-to-last column of Table A.2 illustrates the proposed extended vector of fine sample F' and the construction of the first coarse sample c_1 and detail sample d_1, applicable to one possible balanced multiresolution scheme for each set of filters in the table. Here, we only give the construction of c_1 and d_1 because the remaining pairs of coarse and detail samples can be obtained by subsequent shifts of the filter vectors $\mathbf{a}$ and $\mathbf{b}$ by two fine samples along F' (as shown in Fig. 10, for example). Finally, the last column shows the corresponding extended vectors of coarse samples C' and detail samples D', in addition to the reconstruction of the fine samples in F_l and F_r as defined in Section 5.2. In this column, filter vectors of odd and even width are assumed to have formats similar to $[\ldots \;\; v_{-2} \;\; v_{-1} \;\; v_0 \;\; v_1 \;\; v_2 \;\; \ldots]$ and $[\ldots \;\; v_{-2} \;\; v_{-1} \;\; v_1 \;\; v_2 \;\; \ldots]$, respectively.

Although providing a recipe for choosing the appropriate set of filters for a particular application is not the focus of this article, here we provide a high-level guideline. To decide which set of filters is more suitable for a particular application, a number factors such as smoothness of results, widths of filter vectors, the number of vanishing moments of the associated wavelet function, and the support of underlying basis function are taken into consideration. Firstly, when the visual quality of results is important, a set of filters that provides higher level of smoothness is preferred. Secondly, shorter widths of filter vectors imply faster implementation and if applicable, higher frame rate. An interactive focus+context visualization application like the one demonstrated in this article performs more efficiently if the filter vectors are not too wide. For instance, only one level of balanced decomposition of a $512 \times 512 \times 512$ image using a width-7 $\mathbf{a}$ filter vector in place of a width-4 $\mathbf{a}$ filter vector will take 21×256^3 more multiplications, incurring a 75% increase in the number of multiplications required. Next, higher number of vanishing moments of the associated wavelet function implies wider filter vectors and lesser smoothness of results. However, higher number of vanishing moments allows better approximation of scaling functions, which is desirable in compression applications. Finally, filter vectors that provide compact support lead to better local effects, usually required for applications allowing multiresolution editing.

Daubechies proposed a family of orthogonal wavelets with the highest number of vanishing moments for some expected support but it does not allow for the best smoothness [7]. The filter vectors resulting from this work are asymmetric (see Eq. (B.1), for example). Using a similar idea for construction, Cohen el al. proposed the first family of biorthogonal wavelets, which leads to filter vectors that are symmetric or antisymmetric about their centers [5,8]. The biorthogonal and reverse biorthogonal filters we refer

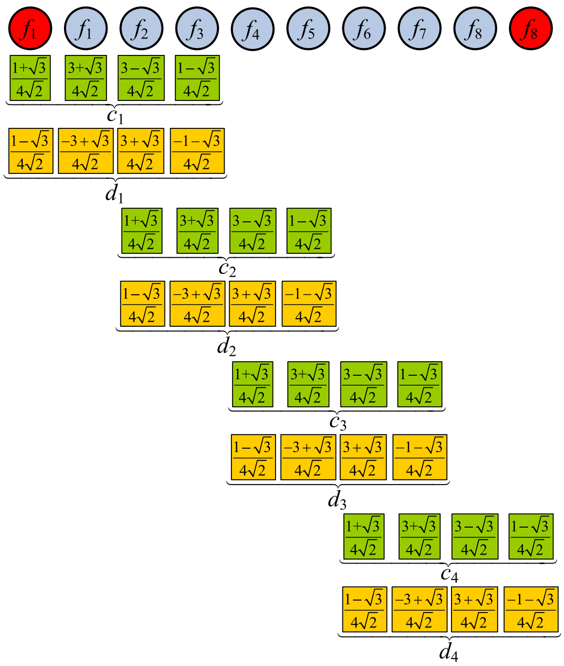

Fig. B.16. Balanced decomposition of 8 fine samples using the decomposition filter vectors **a** and **b** from Eq. (B.1).

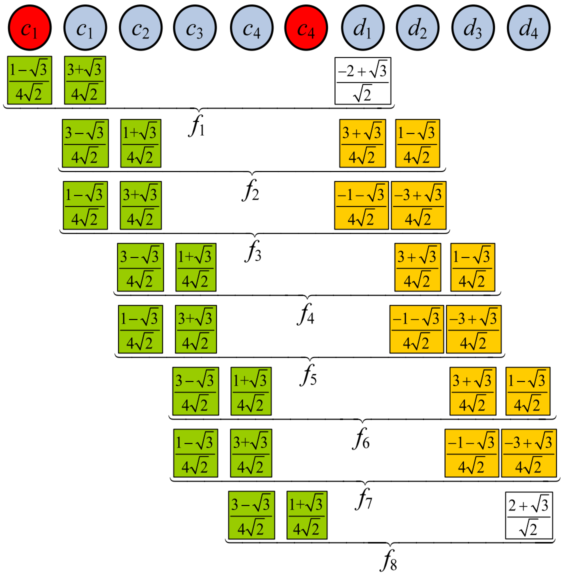

Fig. B.17. Perfect reconstruction of 8 fine samples using the reconstruction filter vectors **p** and **q** from Eq. (B.1).

to in Table A.2 resulted from this work. On the other hand, the B-splines filters in Table A.2 are developed by Samavati et al. based on reverse subdivision [26,3,28]. Filters of higher order B-spline produce smoother results. The associated construction procedure starts by setting the width of the decomposition filter vector **a**, where wider **a** results in better coarse approximations. Constraints can be set in the construction procedure such that the resulting coarse approximations are smoother. For instance, Sadeghi and Samavati proposed smooth reverse subdivision for obtaining smooth coarse data through decomposition [31,32].

Appendix B. An example with asymmetric filter vectors

An attempt to apply our general approach for devising a balanced multiresolution scheme described in Section 5 to Daubechies' asymmetric D4 filters [7,29],

$$\begin{cases} \mathbf{a} = \mathbf{p} = \left[\frac{1+\sqrt{3}}{4\sqrt{2}} \quad \frac{3+\sqrt{3}}{4\sqrt{2}} \quad \frac{3-\sqrt{3}}{4\sqrt{2}} \quad \frac{1-\sqrt{3}}{4\sqrt{2}}\right], \\ \mathbf{b} = \mathbf{q} = \left[\frac{1-\sqrt{3}}{4\sqrt{2}} \quad \frac{-3+\sqrt{3}}{4\sqrt{2}} \quad \frac{3+\sqrt{3}}{4\sqrt{2}} \quad \frac{-1-\sqrt{3}}{4\sqrt{2}}\right], \end{cases} \tag{B.1}$$

produces the balanced decomposition setup shown in Fig. B.16 and the perfect reconstruction setup shown in Fig. B.17. Note that it introduces two extraordinary boundary filter values, $\frac{-2+\sqrt{3}}{\sqrt{2}}$ and $\frac{2+\sqrt{3}}{\sqrt{2}}$ in the reconstruction of f_1 and f_8, respectively. Because the filter vectors in Eq. (B.1) are not symmetric/antisymmetric, the rewriting task suggested in step 2(c) and that of step 3 in our *general construction* given in Section 5.2 were not entirely successful. Therefore, our approach could not ensure a perfect reconstruction using only the regular filters from Eq. (B.1).

As we observe in Fig. B.17, this particular example does not require any extraordinary boundary filters for the subdivision matrix **P**. This may not always be the case while using other asymmetric filter vectors.

References

[1] M.D. Adams, R.K. Ward, Symmetric-extension-compatible reversible integer-to-integer wavelet transforms, IEEE Trans. Signal Process. 51 (10) (2003) 2624–2636.
[2] R.H. Bartels, G.H. Golub, F.F. Samavati, Some observations on local least squares, BIT Numer. Math. 46 (3) (2006) 455–477.
[3] R.H. Bartels, F.F. Samavati, Reversing subdivision rules: local linear conditions and observations on inner products, J. Comput. Appl. Math. 119 (2000) 29–67.
[4] R. Bartels, F. Samavati, Multiresolutions numerically from subdivisions, Comput. Graph. 35 (2) (2011) 185–197.
[5] A. Cohen, I. Daubechies, J.-C. Feauveau, Biorthogonal bases of compactly supported wavelets, Commun. Pure Appl. Math. 45 (5) (1992) 485–560.
[6] G.M. Chaikin, An algorithm for high-speed curve generation, Comput. Graph. Image Process. 3 (4) (1974) 346–349.
[7] I. Daubechies, Orthonormal bases of compactly supported wavelets, Commun. Pure Appl. Math. 41 (7) (1988) 909–996.
[8] I. Daubechies, Ten Lectures on Wavelets, Society for Industrial and Applied Mathematics (SIAM), Philadelphia, PA, USA, 1992.
[9] G. Faber, Über stetige Funktionen, Math. Ann. 66 (1909) 81–94.
[10] D.R. Forsey, R.H. Bartels, Hierarchical B-spline refinement, in: Proceedings of the 15th Annual Conference on Computer Graphics and Interactive Techniques, SIGGRAPH '88, ACM, New York, NY, USA, 1988, pp. 205–212.
[11] S.J. Gortler, M.F. Cohen, Hierarchical and variational geometric modeling with wavelets, in: Proceedings of the 1995 Symposium on Interactive 3D Graphics, I3D '95, ACM, Monterey, CA, 1995, pp. 35–42.
[12] A. Haar, Zur Theorie der orthogonalen Funktionensysteme, Math. Ann. 69 (1910) 331–371.
[13] W.-H. Hsu, K.-L. Ma, C. Correa, A rendering framework for multiscale views of 3D models, in: Proceedings of the 2011 SIGGRAPH Asia Conference, SA '11, ACM, New York, NY, USA, 2011, pp. 131:1–131:10.
[14] E.R.S. Hodges, The Guild Handbook of Scientific Illustration, John Wiley and Sons, Hoboken, NJ, USA, 2003.
[15] H. Kiya, K. Nishikawa, M. Iwahashi, A development of symmetric extension method for subband image coding, IEEE Trans. Image Process. 3 (1) (1994) 78–81.
[16] I. Kharitonenko, X. Zhang, S. Twelves, A wavelet transform with point-symmetric extension at tile boundaries, IEEE Trans. Image Process. 11 (12) (2002) 1357–1364.
[17] E. LaMar, B. Hamann, K.I. Joy, Multiresolution techniques for interactive texture-based volume visualization, in: Proceedings of the 1999 Conference on Visualization, VIS '99, IEEE Computer Society Press, Los Alamitos, CA, USA, 1999, pp. 355–361.
[18] S. Li, W. Li, Shape-adaptive discrete wavelet transforms for arbitrarily shaped visual object coding, IEEE Trans. Circ. Syst. Video Technol. 10 (5) (2000) 725–743.
[19] J. Lin, M.J.T. Smith, New perspectives and improvements on the symmetric extension filter bank for subband/wavelet image compression, IEEE Trans. Image Process. 17 (2) (2008) 177–189.
[20] MATLAB and Wavelet Toolbox Release 2014a, The MathWorks, Inc., Natick, MA, USA, 2014.
[21] Y. Meyer, Ondelettes et Opérateurs, Hermann, 1990.
[22] L. Olsen, F. Samavati, R. Bartels, Multiresolution for curves and surfaces based on constraining wavelets, Comput. Graph. 31 (3) (2007) 449–462.
[23] J. Plate, T. Holtkaemper, B. Froehlich, A flexible multi-volume shader framework for arbitrarily intersecting multi-resolution datasets, IEEE Trans. Visual. Comput. Graph. 13 (6) (2007) 1584–1591.
[24] J. Plate, M. Tirtasana, R. Carmona, B. Fröhlich, Octreemizer: a hierarchical approach for interactive roaming through very large volumes, in: Proceedings of the symposium on Data Visualisation 2002 (VISSYM '02), Eurographics Association, Aire-la-Ville, Switzerland, 2002, pp. 53–60.
[25] J. Sadeghi, Reversing Faber subdivision, Personal communication, 2011.
[26] F.F. Samavati, R.H. Bartels, Multiresolution curve and surface representation: reversing subdivision rules by least-squares data fitting, Comput. Graph. Forum 18 (2) (1999) 97–119.

[27] F.F. Samavati, R.H. Bartels, Local filters of B-spline wavelets, in: Proceedings of the 2004 International Workshop on Biometric Technologies, BT '04, 2004, pp. 105–110.
[28] F.F. Samavati, R.H. Bartels, L. Olsen, Local B-spline multiresolution with examples in iris synthesis and volumetric rendering, in: Image Pattern Recognition: Synthesis and Analysis in Biometrics, Series in Machine Perception and Artificial Intelligence, vol. 67, World Scientific Publishing, 2007, pp. 65–102.
[29] E.J. Stollnitz, T.D. Derose, D.H. Salesin, Wavelets for Computer Graphics: Theory and Applications, Morgan Kaufmann Publishers Inc., San Francisco, CA, USA, 1996.
[30] S. Suter, J.I. Guitian, F. Marton, M. Agus, A. Elsener, C. Zollikofer, M. Gopi, E. Gobbetti, R. Pajarola, Interactive multiscale tensor reconstruction for multiresolution volume visualization, IEEE Trans. Visual. Comput. Graph. 17 (12) (2011) 2135–2143.
[31] J. Sadeghi, F.F. Samavati, Smooth reverse subdivision, Comput. Graph. 33 (3) (2009) 217–225. IEEE International Conference on Shape Modelling and Applications 2009.
[32] J. Sadeghi, F.F. Samavati, Smooth reverse Loop and Catmull-Clark subdivision, Graph. Models 73 (5) (2011) 202–217.
[33] T. Taerum, M.C. Sousa, F.F. Samavati, S. Chan, J.R. Mitchell, Real-time super resolution contextual close-up of clinical volumetric data, in: Proceedings of the Joint Eurographics – IEEE VGTC Symposium on Visualization (EuroVis06), Eurographics Association, May 8–10, 2006, pp. 347–354.
[34] C. Wang, H.-W. Shen, Hierarchical navigation interface: leveraging multiple coordinated views for level-of-detail multiresolution volume rendering of large scientific data sets, in: Proceedings of the Ninth International Conference on Information Visualisation, July 2005, pp. 259–267.
[35] Y.-S. Wang, C. Wang, T.-Y. Lee, K.-L. Ma, Feature-preserving volume data reduction and focus+context visualization, IEEE Trans. Visual. Comput. Graph. 17 (2) (2011) 171–181.
[36] D. Zorin, P. Schröder, W. Sweldens, Interactive multiresolution mesh editing, in: Proceedings of the 24th Annual Conference on Computer Graphics and Interactive Techniques, SIGGRAPH '97, ACM Press/Addison-Wesley Publishing Co., New York, NY, USA, 1997, pp. 259–268.